This is the accepted version of the following article:

Xiaowei Cheng, Xiaodong Ji*, Ziguo Xu, Sheng Gao, Longhe Xu,Seismic behavior of slender prestressed reinforced concrete short-leg walls, Journal of Building Engineering, 56, 2022, 104710,

which has been published in final form at [Link to final article]

Seismic Behavior of Slender Prestressed Reinforced Concrete Short-Leg Walls

Xiaowei Cheng[a], Xiaodong Ji[b*], Ziguo Xu[c], Sheng Gao[d], Longhe Xu[e]

*[a]Lecturer, Key Laboratory of Urban Security and Disaster Engineering of Ministry of Education, Beijing University of Technology, Beijing 100124, China;*

*[b]Associate professor, Key Laboratory of Civil Engineering Safety and Durability of China Education Ministry, Department of Civil Engineering, Tsinghua University, Beijing 100084, China*

*[c]Researcher, RBS Architectural Engineering Design Associates Beijing Branch, Beijing 100022, China;*

*[d] Researcher, Institute of Engineering Mechanics, China Earthquake Administration, Hebei 101601, China;*

*[e]Professor, Beijing Jiaotong University, Beijing 100044, China;*

**Abstract:** To reduce the possible adverse effects of axial tensile force on reinforced concrete (RC) walls, bonded prestressed concrete (PC) walls are recommended for use in high-rise buildings. These could offer an initial axial compressive load to balance the possible axial tensile force of a RC wall induced by strong ground motions. In this study, three PC short-leg walls with a high-aspect-ratio of 2.0 were tested for various loading patterns, including constant axial forces and variable axial forces, combined with cyclic shear loading. Test results indicated that failure modes varied with loading patterns, including flexure-shear failure (coupled constant axial tension and cyclic shear loading), shear compression failure (coupled constant axial compression and cyclic shear loading), and flexure failure (coupled variable axial forces and cyclic shear loading). Variable axial forces led to the normalized tension-shear strength and compressive-shear strength of PC short-leg walls decreasing by 8.5% and 9.1%, respectively, and the tension-shear ultimate ratio decreasing by 35%. The ultimate drift ratio of PC short-leg walls ranged from 1.8% to 3.7%. Variable axial loads decreased the pre-yield secant stiffness in tension-shear and compression-shear loading, while the influence on post-yield secant stiffness was less pronounced. Variable axial forces did not increase the maximum crack width of PC short-leg walls, but clearly decreased the accumulated energy of PC short-leg walls as they changed the shape of hysteretic curves. Finally, a finite element model of PC short-leg walls was developed and the accuracy of the model was evaluated using experiment results, including its hysteretic characteristics and lateral displacement profiles.

**Keywords:** Bonded prestressed concrete wall; variable axial forces; high-aspect-ratio; strength; finite element model.

## 1. Introduction

Shear walls are the typical major lateral load-carrying components in high-rise buildings due to their high lateral strength and stiffness. Under strong ground motions, some reinforced concrete (RC) shear walls may be subjected not only to a constant vertical compressive load from gravity but also to combined variable axial forces (from compression to tension), moments, and shear forces. For instance, in a coupled wall system with a high coupling ratio, the axial forces induced by coupling beam shears may result in the wall pier sustaining a net axial tensile force, combined with shear and bending actions induced by lateral loading, as illustrated in Fig. 1(a). Other examples are core wall or slender shear wall structures, as depicted in Fig. 1(b) and (c), where the peripheral walls may be subjected to the tensile forces caused by an overturning moment from lateral loading. Such coupled axial tension-shear action is a critical loading condition for RC walls and may lead to significant structural damage, as identified by past earthquake reconnaissance (e.g., 2010 Chile earthquake [1] and experimental tests of core wall systems [2]).

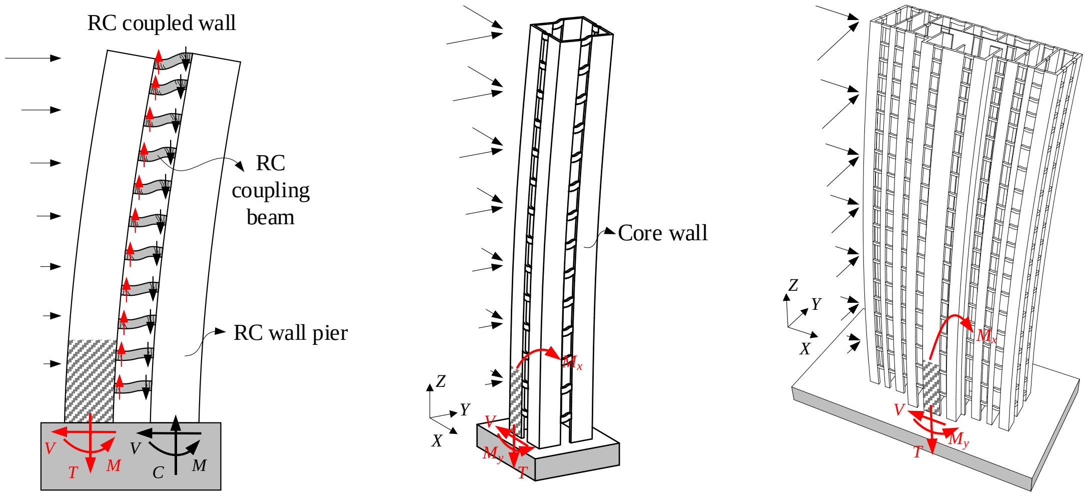


(a) Coupled wall (b) Core wall (c) Shear wall structure

**Fig. 1.** RC walls undergoing combined axial tension, bending moment and shear force.

Past research on RC walls subjected to constant axial tensile force and cyclic shear loading found that axial tension significantly decreased the lateral stiffness and strength of RC walls [3,4,5,6,7,8,9], resulting in a redistribution of lateral force among the walls. To prevent the adverse impact of large axial tensile forces, the Chinese Technical Guideline of Peer Review for Seismic Design of Super-Tall Buildings [10] specifies a strict limit on the axial tensile force of RC walls. According to this guideline, under design basis earthquakes (DBEs), the nominal tensile stress of RC walls ($\sigma_n = N/A_g$) should be less than the tensile strength of concrete, where $N$ and $A_g$ are the axial tensile force and gross cross-sectional area of the wall section, respectively. Otherwise, the steel-concrete composite walls (e.g., steel reinforced concrete (SRC) walls and steel-plate composite walls) [11,12,13] are recommended for use instead of RC walls. Notably, in Chinese practical construction, steel-concrete composite walls are often used for thick walls but seldom used for thin walls; this is because slender steel profiles present difficulties in terms of their positioning, erection, and connection. This research proposed another promising alternative approach using bonded prestressed concrete (PC) walls. The prestressedstrands in PC walls can provide an initial axial compressive load to balance the possible axial tensile force of walls induced by strong ground motions, thus controlling the development of cracks and enhancing the lateral strength and stiffness of the walls. It is important to note that this kind of prestressed concrete approach is probably not suitable for walls subjected to a high axial compressive force. This is due to the additional axial compression induced by prestressed strands would further increase the axial compressive force ratio and decrease the ductility of structural walls.

While a number of precast unbonded post-tensioned concrete walls have been studied in recent years [14,15,16], literature on the seismic behavior of bonded PC short-leg walls is extremely limited. Thus, the objective of this study was to investigate the seismic behavior of bonded PC short-leg walls subjected to various types of loading pattern. An experimental program was conducted in which three PC short-leg walls with a larger-aspect-ratio of 2.0 were tested for different loading patterns, including constant axial forces and variable axial forces (ranged from compression to tension), combined with cyclic shear loading. The test results were detailed in terms of failure modes, hysteretic response, strength and stiffness, deformation capacities, deformation components, crack width, and axial deformation. Additionally, a finite element (FE) model was developed using OpenSees software to simulate the hysteretic behavior of PC short-leg walls under the various types of loading pattern.

## 2. Experimental Program

### *2.1. Details of test walls*

A typical residential building located in Xi'an, China, with a total height of 138.6 m served as a prototype building to guide the design of test wall specimens. The sectional depth and thickness of the prototype wall in the lower stories of the residential building were 3.0 m and 1.0 m, respectively. It needs to note that the prototype wall is a part of a T-shaped wall in the short side direction and had a low sectional depth-to-thickness ratio of 3. Such walls with a depth-to-thickness less than 8.0 are defined as short-leg walls according to Chinese technical specification for concrete structures of tall building (JGJ 3-2010) [17]. The test wall specimens were fabricated to approximately 1/4 scale of the prototype wall, with a length and thickness of 0.72 m and 0.24 m, respectively. A total of three wall specimens (labeled HPCW0, HPCW1 and HPCW2) were designed, each with identical geometric dimensions, as depicted in Fig. 2. The clear height of the test specimens was 1.44 m, resulting in a shear-to-span ratio of 2.0.

A top beam and foundation beam were fabricated together with the wall to allow for load application and anchorage of the wall specimen to reaction floor. The foundation beam was fabricated first, followed by construction of the wall and top beam. A total of twelve D14 (diameter of 14 mm) steel reinforcing bars were used as longitudinal reinforcement for each boundary element, corresponding to a 3.94% reinforcement ratio. The vertically distributed reinforcement in the wall web comprised D6 steel rebars at a spacing of 90 mm, corresponding to a 0.26% reinforcement ratio. The horizontally distributed reinforcement comprised D6 steel rebars at a spacing of 85 mm, corresponding to a 0.28% reinforcement ratio. The boundary transverse reinforcement consisted of D8 steel rebars fabricated as rectangular hoops with a vertical spacing of 70 mm, corresponding to a 2.60% volumetric transverse reinforcement ratio. In addition, a total of seven D15.2 (nominal diameter = 15.2 mm) strands were arranged along the wall length. The strands were installed in corrugated steel pipes (CSP) cast together with the wall body. Fasteners and nuts were used at the two ends of the strands to apply post-tension forces. Having applied these forces to the strands, a high strength grouting material was injected into the corrugated steel pipe from the reserved holes in the foundation (see Fig. 2(b)) to enhance the connection between the strands and surrounding concrete.

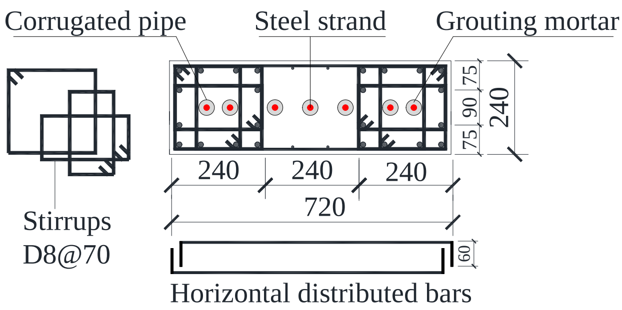


(a) Cross section

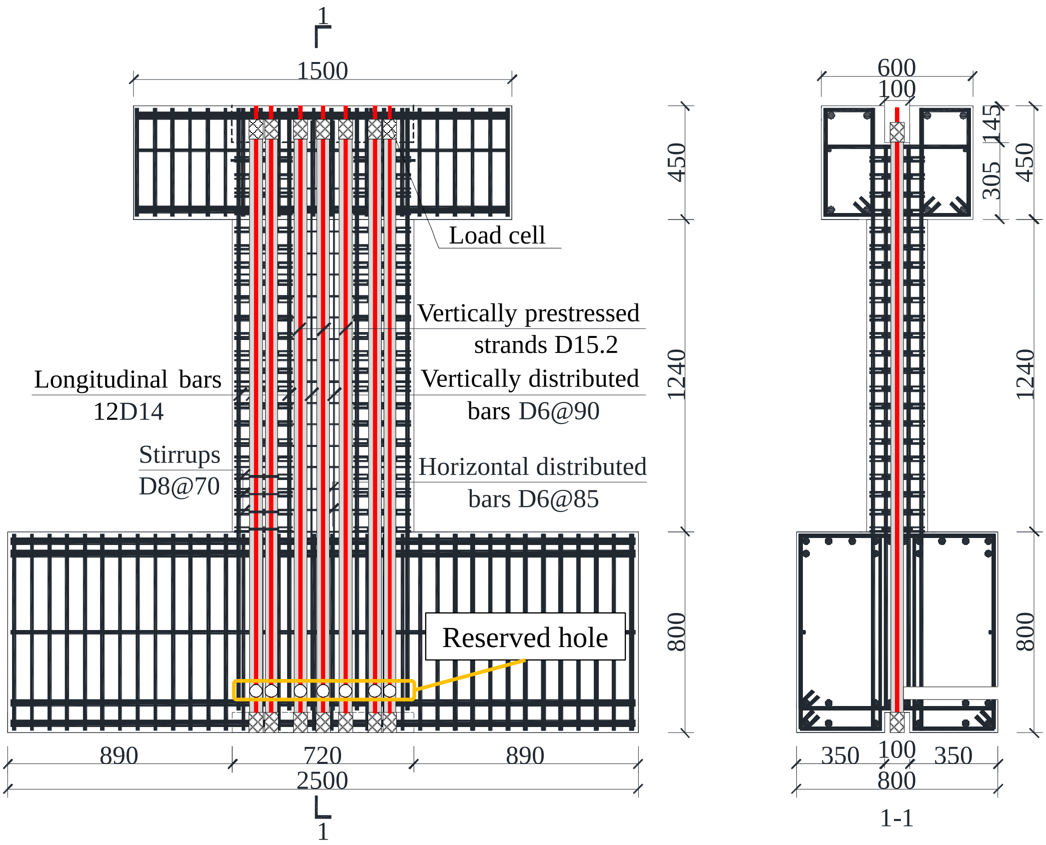


(b) Elevation view

**Fig. 2.** Geometry and reinforcement of specimens (units: mm).

## *2.2. Material properties*

The strength grade of the concrete used in these wall specimens was C50 (nominal cubic compressive strength $f_{cu,n}$ = 50 MPa). However, the average compressive strength obtained from standard 150 mm cubes $f_{cu}$ on the test day was 60.0, 54.2, and 66.1 MPa for specimens HPCW0, HPCW1, and HPCW2, respectively. The axial compressive strength of concrete $f_c$ and axial tensile strength of concrete $f_t$ were assumed to be $0.76f_{cu}$ and $0.395f_{cu}^{0.55}$, respectively in accordance with the Chinese Code for Design of Concrete Structures GB 50010-2010 [18].

Grade HRB400 (nominal yield strength $f_{y,n}$ = 400 MPa) and G1860 (nominal yield strength $f_{y,n}$ = 1860 MPa) were used for reinforcement and strands. Table 1 summarizes the properties of the reinforcement and strands, which were the average values obtained from three standard coupon tests. The ultimate strength and uniform elongation (i.e., measured strain corresponding to the peak stress) listed in this table are also the average values measured from three standard coupon tests.

**Table 1.** Material properties of reinforcement and strand.

| | Diameter (mm) | Yield strength $f_y$ (MPa) | Ultimate strength $f_u$ (MPa) | Uniform elongation $\delta$ (%) |
|---|---|---|---|---|
| Reinforcement | 6 | 454 | 690 | 13.7 |
| | 8 | 500 | 749 | 10.9 |
| | 14 | 480 | 665 | 13.3 |
| Strand | 15.2 | 1801 | 1869 | 3.0 |

*2.3. Test setup and instrumentation*

The test setup is presented in Fig. 3. The foundation beam was anchored to the strong reaction floor, and the top beam was connected to three hydraulic actuators. The two vertical hydraulic actuators were used to apply axial loads, while one horizontal hydraulic actuator was used to apply cyclic shear loads. An out-of-plane support was used to prevent out-of-plane displacement and twisting of the wall during testing. The horizontal loading centroid was 1.44 m from the wall base, resulting in a shear-to-span ratio of 2.0 for wall specimens.

Load cells were utilized to measure the applied axial loads and lateral loads. Twenty-one linear variable differential transformers (LVDTs) were utilized to measure the displacement at different locations of the wall, as shown in Fig. 4(a). The configuration of LVDTs made it possible to determine the global displacement of the wall (LVDTs D1 and D2), wall average vertical strains and flexure deformations (LVDTs from D5 to D10), wall shear deformation (LVDTs from D11 to D14), possible rotation and slip of foundation beam (LVDTs from D15 to D17), vertical strain distribution over the cross-section at the wall bottom (LVDTs D5, D18 to D20, and D8), and wall axial deformation (LVDTs D21). Fifteen strain gauges were used to monitor the strains on reinforcement and strands, as depicted in Fig. 4(b).

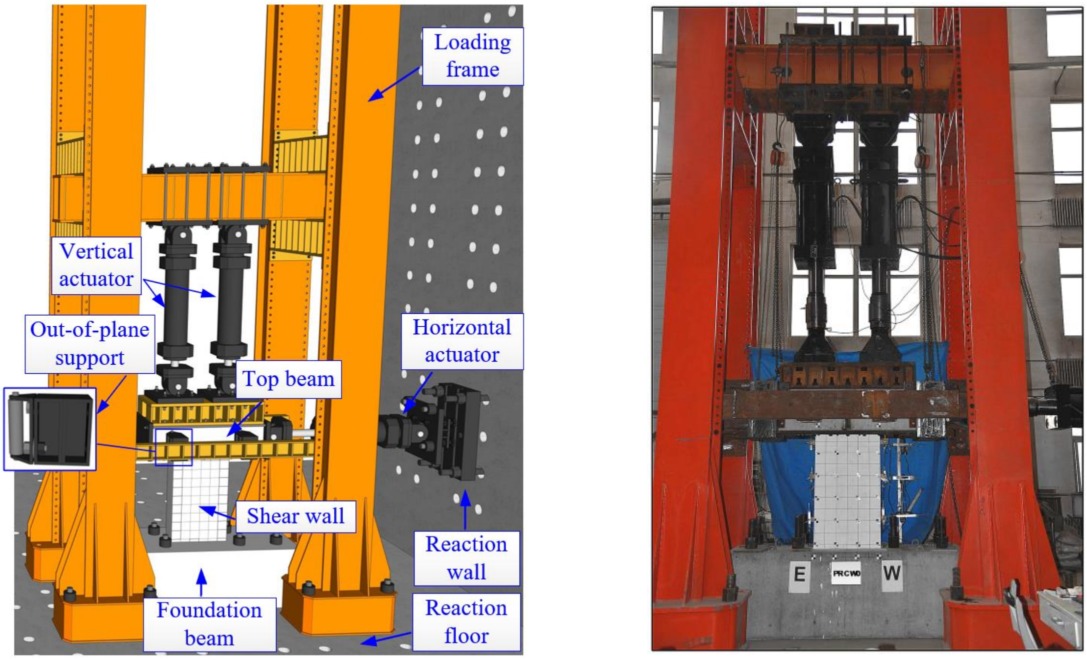


(a) Schematic drawing (b) Photograph

**Fig. 3.** Test setup.

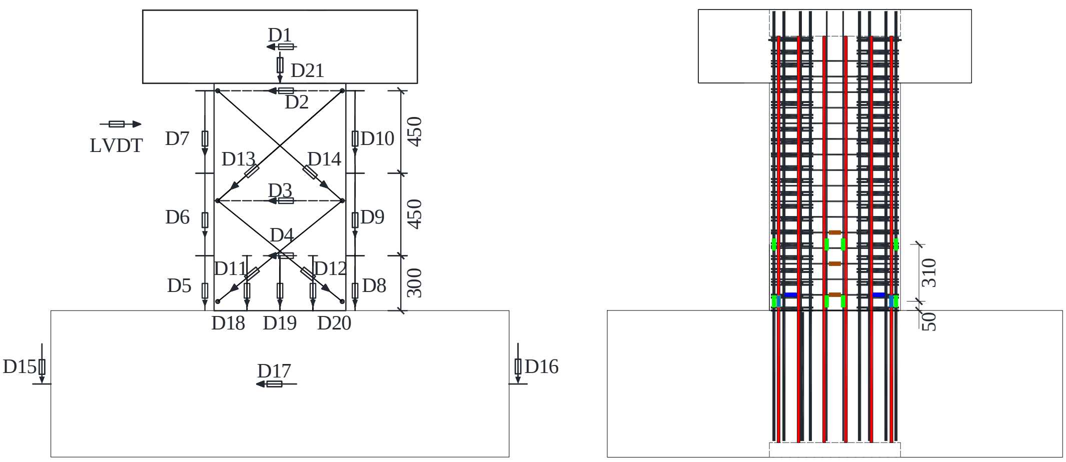

(a) Displacement transducers (b) Strain gauges

**Fig. 4.** Layout of instruments.

*2.4 Loading protocol*

Two types of loading protocol were considered in the test program, details of which are as follows.

**Specimens HPCW0 and HPCW2:** A constant axial tensile force $N_t$ was applied to specimen HPCW0 while a constant axial compressive force $N_c$ was applied to specimen HPCW2. The values of $N_t$ and $N_c$ are presented in Table 2. As depicted in Fig. 5(a), prior to yielding of the specimen, two levels of lateral drift with one cycle at each drift level were applied to the wall. After the specimen reached the predicted yield drift $\Delta_{y,p}$ corresponding to 0.3% drift ratio, lateral displacement was increased at the predicted yield drift increments, with two cycles at each drift level. Note that the preliminary FE analysis using Opensees software was conducted to predict the lateral force-displacement curve of the specimen and the predicted yield drift was determined using the idealized force-displacement curve method in accordance with ASCE/SEI 41-13 [19]. During the test, loading to the west direction was defined as positive loading and loading to the east as negative loading. The test terminated when the lateral load capacity of the wall fell below 85% of the lateral peak load or when the wall could not sustain the axial force due to fracture of reinforcement or crushing of boundary concrete.

**Specimen HPCW1** was subjected to coupled variable axial forces and cyclic shear loading. The loading pattern was designed to mimic the loading history of a wall pier in a coupled wall system under cyclic pushover loads, as detailed in Reference [20]. One wall pier sustained increased axial tensile force induced by coupling beam shears along with an increased lateral drift; the axial tensile force then remained constant after all coupling beams yielded, despite further increase in lateral drift. When the pushover force was reversed, the wall pier sustained axial compressive force induced by the reversed shear forces of the coupling beam. Fig. 5(b) presents the relationship between axial force and cyclic lateral drift applied to the specimen. Positive loading is used as an example to illustrate the loading protocol. First, an initial axial compressive force $N_g$, representing the gravity load, was applied to the wall. Prior to the predicted yield drift $\Delta_{y,p}$, the axial load varied linearly with the applied lateral drift from $N_g$ at zero drift to the targeted axial tensile force $N_t$ at drift $\Delta_{y,p}$ (see the *OA* phase in Fig. 5(b)). Two levels of lateral drift (i.e., P1 and P2 point in Fig. 5(b)) with one cycle at each drift level were used in this loading stage. After the specimen yielded, the axial tensile force was maintained at a constant value of $N_t$ until the lateral drift attained the targeted lateral drift (e.g., $m\Delta_{y,p}$), as depicted in the *AB* phase in Fig. 5(b). For the unloading phase, the axial force unloaded linearly from the targeted axial tensile force $N_t$ to the initial axial compressive force $N_g$ at the lateral drift decreased to $(m-1)\Delta_{y,p}$, as depicted in the *BC* phase in Fig. 5(b). The initial axial compressive force $N_g$ was then maintained at a constant level and the lateral drift decreased further to zero, as illustrated in the *CO* phase in Fig. 5(b). The loading process in the negative loading direction was similar to that in the positive loading direction. The history of cyclic lateral drifts for specimen HPCW1 was identical to that for specimens HPCW0 and HPCW2, as presented in Fig. 5(a). The entire loading process including the application of axial load and cyclic lateral load was controlled by program.

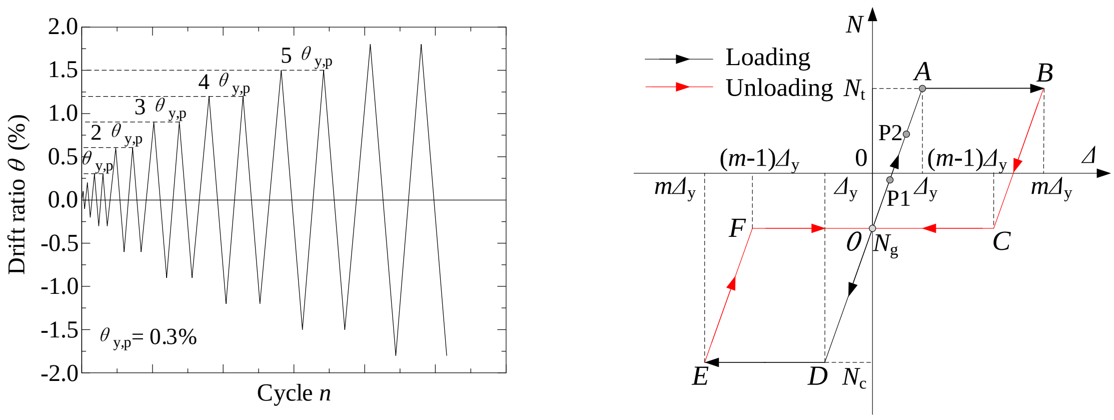


(a) Cyclic shear loading history

(b) Combined variable axial load and cyclic lateral loading

**Fig. 5.** Loading protocol for all test wall specimens.

The values of axial loads $N_g$, $N_t$ and $N_c$ applied to the wall specimens were obtained from pushover analysis of the walls in the prototype building, and are listed in Table 2. The prototype walls were estimated to have a tensile force demand of approximately $N_t = 3A_g f_{tk}$ under design basis earthquakes (DBEs), where $A_g$ denotes the gross cross-sectional area of the wall and $f_{tk}$ denotes the standard value of the tensile strength of concrete. Because the Chinese Technical Guideline of Peer Review for Seismic Design of Super-Tall Buildings requires the nominal tensile stress of RC walls ($\sigma_n = N/A_g$) to be less than the value of $f_{tk}$, the prestressed force of the prototype wall was determined as $N_p$=2$A_g f_{tk}$, thus ensuring that the remaining net tensile force of the wall section did not exceed $A_g f_{tk}$. The values of loads applied to the wall specimens were scaled from the prototype wall loads. Axial compressive force ratio $n_c = N/(A_g f_c')$ and normalized concrete tensile stress $n_t = N/(A_g f_t)$ were used to quantify the magnitude of the axial force, where $A_g$ denotes the gross cross-section of the wall, and $f_c'$ and $f_t$ denote the axial compressive strength and tensile strength of concrete, respectively. The gravity load $N_g$ of HPCW2 corresponded to an axial compressive force ratio $n_c$ = 0.14, while the total value of

$n_{c,tot}$ reached 0.24 when the prestressed force was included. At an axial compressive load of $N_c$ = 3022 kN, the total axial compressive force ratio $n_{c,tot}$ reached 0.45. Although the axial tensile load led to a large normalized concrete tensile stress $n_t$ = 2.0, the net normalized concrete tensile stress $n_{t,\,tot}$ was reduced to 0.67 when the load balanced by the prestressed force was excluded. Due to the strong boundary element, the calculated in-plane tension-flexural and compression-flexural strength of the overall wall specimen were approximately 2.0 and 1.5 times its in-plane shear strength. The flexural strength of the PC short-leg wall was assessed from cross-section analysis using the XTRACT [21] program and the measured material properties , while the shear strength was calculated using ACI 318-19 [22] equations presented later in the paper.

**Table 2.** Values of axial load applied for wall specimens.

| Spec. no | Prestressed force | Initial axial force | | | Targeted axial compressive force | | | Targeted axial tensile force | | |
|---|---|---|---|---|---|---|---|---|---|---|
| | $N_p$ (KN) | $N_g$ (KN) | $n_c$ | $n_{c,tot}$ | $N_c$ (kN) | $n_c$ | $n_{c,tot}$ | $N_t$ (kN) | $n_t$ | $n_{t,tot}$ |
| HPCW0 | | | 0.15 | 0.27 | | 0.38 | 0.50 | | 2.1 | 0.70 |
| HPCW1 | -912 | -1197 | 0.17 | 0.30 | -3022 | 0.42 | 0.55 | 1369 | 2.2 | 0.74 |
| HPCW2 | | | 0.14 | 0.24 | | 0.35 | 0.45 | | 2.0 | 0.67 |

Note: The values of $n_c$ and $n_t$ do not consider the contribution of the prestressed force, whereas the values of $n_{c,tot}$ and $n_{t,tot}$ do consider this contribution.

## 3. Experimental results

### *3.1. Observed damage and failure modes*

The following sections describe the experimentally observed behavior of each wall specimen based on visible damage (cracking, spalling, crushing, buckling, fracture, etc.).

***Specimen HPCW0:*** This specimen was tested under the combined constant axial tensile force and cyclic lateral loading. Horizontal cracks with a maximum width of 0.15 mm were observed at the east wall boundary after the application of axial tensile force, as presented in Fig. 6(a). It needs to note that although the axial tensile forces applied by two vertical actuators were identical in the test, horizontal cracks were mainly observed at the east boundary and wall web. Analysis of the measured displacement data (LVDTs D15 and D16 in Fig. 4(a)) indicates that the foundation beam had a slight rotation during the application of axial tensile forces due to non-uniformly distributed restraint forces provided by the anchorage bolts, which led to an additional bending moment on the wall. The additional bending moment induced an increased tensile demand on wall's east boundary than the west boundary, thus resulting in unsymmetrical distribution of cracks. At 0.1% lateral drift, horizontally flexural cracks with a maximum width of 0.15 mm were observed at both wall boundaries. At approximate 0.3% lateral drift, boundary longitudinal reinforcement yielded, followed by the development of inclined cracks with a maximum width of 0.40 mm on the wall web during the loading cycle to 0.6% lateral drift, as depicted in Fig 6(b). Thereafter, the width of inclined cracks increased noticeably and diagonal compressive struts from the boundary element to the wall web were observed, following which a peak lateral load was reached at 2.7% lateral drift, as shown in Fig. 6(c). At the peak load, the boundary core concrete did not significantly damage, and the measured strain indicated that the boundary transverse reinforcement had not yielded yet. Upon further increased drift loading, gradual strength degradation was observed due to the crushing and spalling of wall web concrete. When loading to a 3.9% lateral drift, flexure-shear failure occurred and the lateral load dropped to 85% of peak load due to serious spalling of web concrete along the diagonal compressive struts near the boundary element-web interface, as illustrated in Fig. 6(d). Importantly, no obvious spalling and crushing of cover concrete was observed in either wall boundary for specimen HPCW0, as presented in Fig. 6(d).

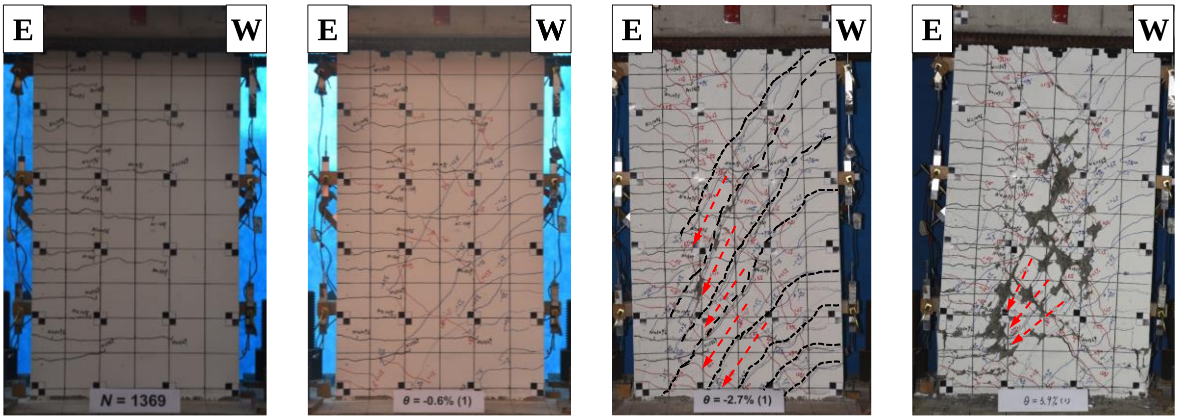


(a) $N$=1369 kN (b) $\theta$ = -0.6 % (c) $\theta$ = -2.7 % (d) $\theta$ = 3.9 %

**Fig. 6.** Photographs of specimen HPCW0: (a) After applying axial tensile force; (b) 0.6% lateral drift; (c) Peak lateral load; (d) End of testing.

The reinforcement strain also reflects the progressive failure of specimen HPCW0. Fig. 7 depicts the measured strain of boundary longitudinal reinforcement (at the east wall boundary end) and horizontally distributed reinforcement (at the 450 mm height above the wall foundation). Before an approximate 1.5% lateral drift, the variation of horizontally distributed reinforcement strain was relatively small (as shown in Fig. 7(b)) and the tension strain of boundary longitudinal reinforcement was close to linearly increasing as top displacement increased (as illustrated in Fig. 7(a)). This indicated that the flexural mechanism dominated the lateral behavior in this loading stage. During an approximate 1.5%-2.1% lateral drift, the tension strain of boundary longitudinal reinforcement continuously increased and there was a sudden increase in the tension strain of horizontally distributed reinforcement. Thereafter, the tension strain of boundary longitudinal reinforcement steadily decreased as top displacement increased while the strain of horizontally distributed reinforcement further increased and attained a tension strain of approximately 0.3%, indicating that shear mechanism dominated the lateral behavior in this stage. Notably, the strain gauges did not work when the strain approximated 0.3% (this phenomenon also observed in the following sections). These observations are consistent with the definition of flexure-shear failure which comprises flexural-control behavior before yielding, followed by shear failure at a larger drift ratio [23].

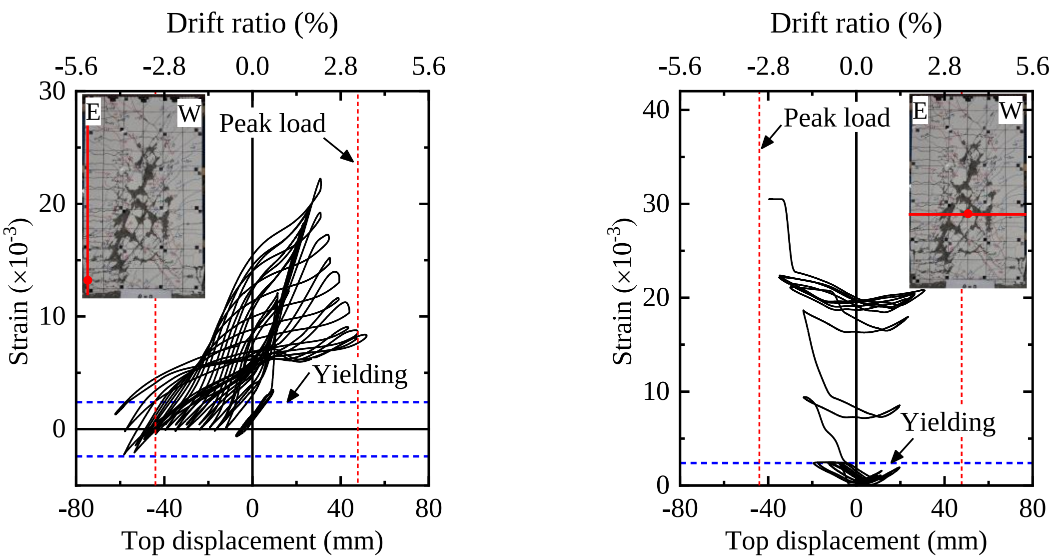


(a) Boundary longitudinal reinforcement (b) Horizontally distributed reinforcement

**Fig. 7.** Strains of reinforcement in specimen HPCW0.

***Specimen HPCW2:*** This specimen was tested under the combined constant axial compressive force and cyclic lateral loading. Horizontally flexural cracks with a maximum width of 0.05mm were observed at both wall ends during the first cycle to 0.2% lateral drift. As lateral drift increased, inclined cracks developed on each side of the wall, extending from the wall top corner toward the wall bottom corner at another side at 0.6% drift, as shown in Fig.

8(a). The angle of inclined cracks was steeper and the distribution of inclined cracks was sparser than that of specimen HPCW0 because specimen HPCW2 had a high compressive force. At a drift ratio of 0.9% in negative loading, multiple vertical cracks were observed at an approximate 200 mm height of the west wall boundary end. When loading to 1.2% lateral drift, the wall specimen attained peak lateral load after the width of inclined cracks increased significantly, and there was slight spalling of cover concrete at both wall boundaries adjacent to the wall-foundation block interface, as presented in Fig. 8(b). During the loading cycle to 2.1% lateral drift, concrete in the core of both wall boundaries crushed and the cover concrete of the wall web spalled, which initiated shear compression failure and a fall in lateral load to 85% of peak load, as depicted in Fig. 8(c)-(d). The measured strain indicated that the boundary transverse reinforcement reached 0.0026 at the peak load and 0.0058 at the final failure (yield strain of boundary transverse reinforcement is 0.0025), indicating significant development of confining effect to the core concrete. Furthermore, although HPCW2 had a high axial compressive force ratio (the true axial compressive ratio was 0.45), no obvious buckling of longitudinal reinforcement was observed during the tests until failure occurred.

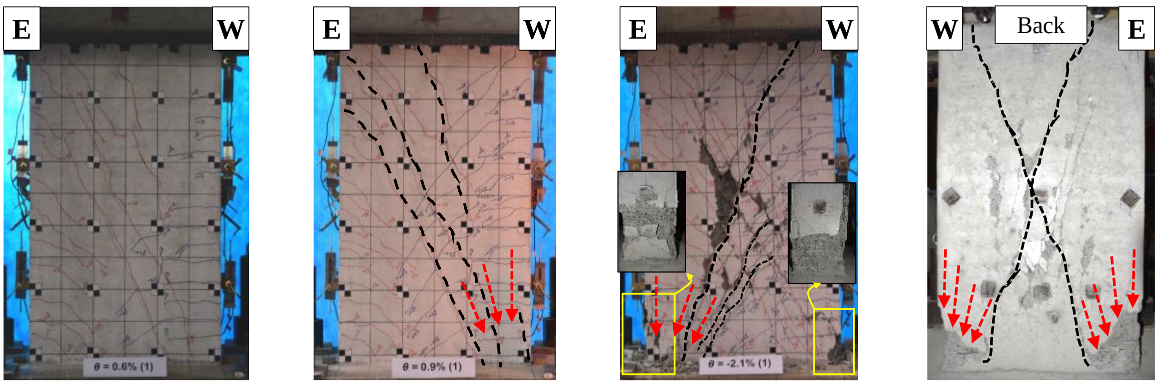


(a) $\theta = 0.6$ %　(b) $\theta = 1.2\%$　(c) $\theta = 2.1$ %　(d) $\theta = 2.1\%$

**Fig. 8.** Photographs of specimen HPCW2: (a) 0.6% lateral drift; (b) Peak lateral load; (b)

End of testing; (d) Back face of the wall at the end of testing.

Fig. 9 depicts the measured strain of boundary longitudinal reinforcement and horizontally distributed reinforcement in specimen HPCW2. Due to the high axial force ratio, the boundary longitudinal reinforcement of specimen HPCW2 was in compression (negative value) and the compressive strain was close to changing linearly as top displacement varied, as illustrated in Fig. 9(a). The strain of horizontally distributed reinforcement exhibited a more rapid increase than that of boundary longitudinal reinforcement due to the fast development of incline cracks and shear compression failure, as shown in Fig. 9(b).

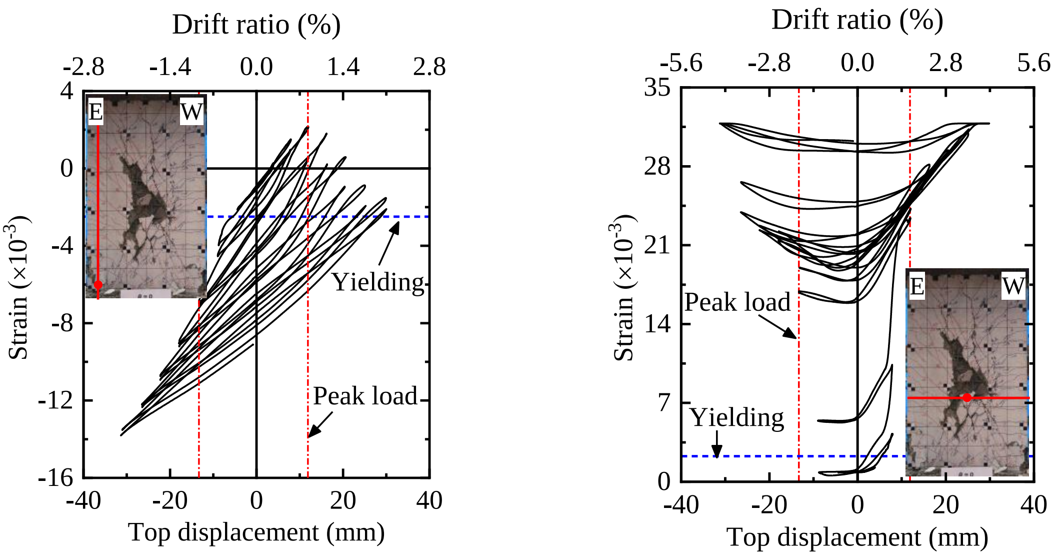


(a) Boundary longitudinal reinforcement (b) Horizontally distributed reinforcement

**Fig. 9.** Strains of reinforcement in specimen HPCW2.

***Specimen HPCW1:*** This specimen was tested under the combined variable axial load and cyclic lateral loading. The axial load was tension in the pull direction (positive loading) and compression in the push direction (negative loading). Horizontally flexural cracks with a maximum width of 0.1 mm were observed at the east wall boundary at 0.2% lateral drift in positive loading (under coupled axial tension-shear loading to the west direction). When loading to a 0.6% lateral drift, inclined cracks with a maximum width of 0.2 mm developed from the boundary zone and extended toward the wall web, as presented in Fig. 10(a), which was similar to what happened to the HPCW0. At a lateral drift of 0.9% in negative loading (under coupled axial compression-shear loading to the east direction), multiple vertical cracks were observed at approximately 150 mm height of the east wall boundary end, followed by minor spalling of cover concrete at the wall end. The specimen attained peak lateral load at 1.2% lateral drift in negative loading due to crushing and spalling of cover concrete at the east wall boundary, as illustrated in Fig. 10(b). When the wall was loaded in the compression-shear direction to a 2.4% lateral drift, serious crushing of core concrete at the east wall boundary and buckling of longitudinal reinforcement occurred. The measured strains of the boundary transverse reinforcement reached 0.0039 at the peak load and 0.014 at the final failure. This initiated flexure failure during the first cycle to a 3.0% lateral drift in the tension-shear direction due to fracture of boundary longitudinal reinforcement in the east wall boundary, as depicted in Fig. 10(c)-(d).

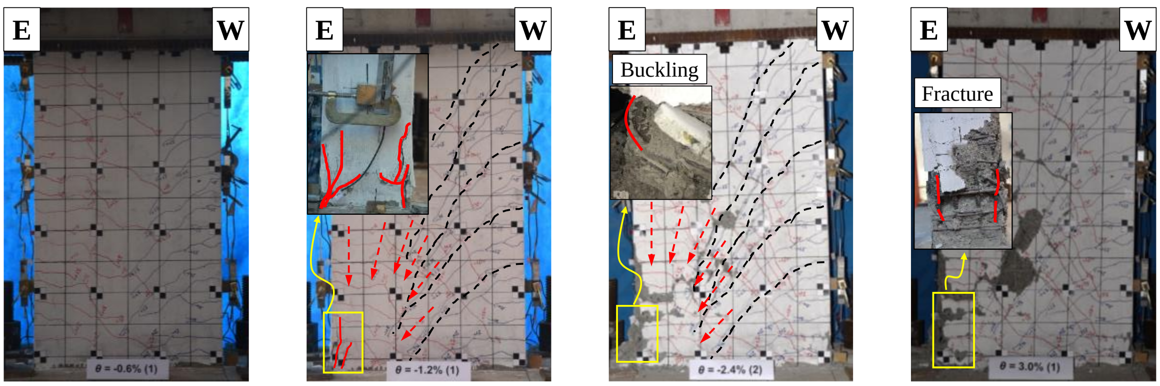


(a) $\theta$ = -0.6 % (b) $\theta$ = -1.2 % (c) $\theta$ = -2.4 % (d) $\theta$ = 3.0%

**Fig. 10.** Photographs of specimen HPCW1: (a) 0.6% lateral drift; (b) Peak lateral load in the negative loading; (c) Buckling of reinforcement; (d) Fracture of boundary reinforcement.

Fig. 11 presents the measured strain of boundary longitudinal reinforcement and horizontally distributed reinforcement in specimen HPCW1. Prior to compression-shear peak load, the strain variation of horizontally distributed reinforcement was relatively small (as shown in Fig. 11(b)) and the strain of boundary longitudinal reinforcement was close to changing linearly as top displacement varied (as depicted in Fig. 11(a)), indicating that the flexural mechanism dominated the lateral behavior in this loading stage. Following compression-shear peak load, the compression strain of boundary longitudinal reinforcement steadily decreased due to buckling of the boundary longitudinal reinforcement. It is important to note that although specimen HPCW1 and HPCW2 exhibited an approximately compressive strain in boundary longitudinal reinforcement, buckling of boundary longitudinal reinforcement was observed for specimen HPCW1 because a large tensile strain developed in the longitudinal reinforcement during positive loading (coupled axial tension-shear loading), as illustrated in Fig. 11(a). The strain of horizontally distributed reinforcement significantly increased after compression-shear peak load due to the development of incline cracks, as shown in Fig. 10(b)-(c).

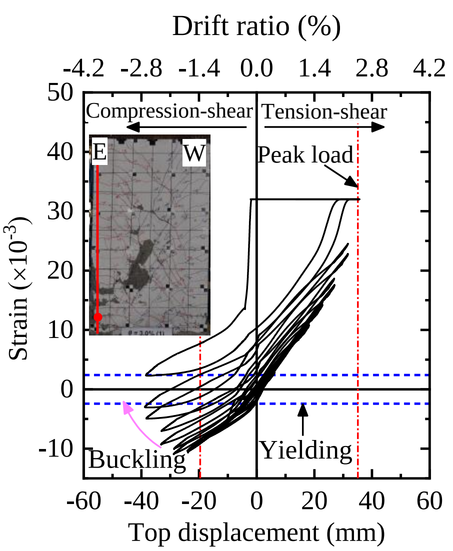


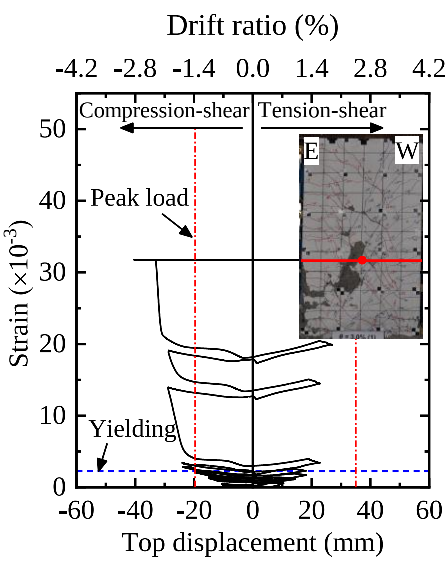

(a) Boundary longitudinal reinforcement (b) Horizontally distributed reinforcement

**Fig. 11.** Strains of reinforcement in specimen HPCW1.

It is important to note that the classification of failure modes in this study was based on these rules proposed by Paulay and Priestley [24] and specifications in JGJ 3-2010 (China code) [17]. Flexure failure is characterized by cracking of concrete at plastic hinge zone, yielding of boundary longitudinal reinforcement, and then crushing of concrete or fracture of boundary longitudinal reinforcement. Flexure-shear failure is characterized by flexural cracking at the plastic hinge zone, yielding of boundary longitudinal reinforcement in tension, and then yielding of horizontal shear reinforcement and spalling of wall web concrete. The flexure-shear failure was indicated where flexural yielding was followed by shear failure at a large drift ratio [23]. Paulay and Priestley [24] classified the shear failure into diagonal tension failure, diagonal compression failure and sliding shear failure. Diagonal tension failure is generally observed in walls with insufficient horizontal shear reinforcement and is characterized by corner-to-corner diagonal crack, yielding or fracture of horizontal shear reinforcement. Diagonal compression failure is triggered by crushing of the diagonal compression struts in a wall with adequate shear reinforcement, of which the average shear stress is high. However, according to JGJ 3-2010, diagonal compression failure is further classified into diagonal compression failure and shear-compression failure based on whether the horizontal shear reinforcement yields or not. If the horizontal shear reinforcement does not yield, diagonal compression failure classified by Paulay and Priestley is also defined as diagonal compressive failure in JGJ 3-2010. If the horizontal shear reinforcement yields, diagonal compression failure classified by Paulay and Priestley is defined as shear-compression failure in JGJ 3-2010. Sliding shear failure often occurs because the yielding of vertical reinforcement (leading to an open crack at wall base) and concrete crushing (spreading along the wall length) lead to a weak sliding surface under the force or displacement reversal.

For specimen HPCW0, flexural cracking of boundary concrete and yielding of boundary longitudinal reinforcement was observed firstly (caused by flexure mechanism), followed by the development of inclined cracks, yielding of horizontal shear reinforcement, and spalling of web concrete (caused by shear mechanism), as shown in Fig. 6. Therefore, the failure mode of HPCW0 was defined as flexure-shear failure. For specimen HPCW2 that had a high axial compressive force ratio of 0.45, shear cracks were firstly developed on each side of the wall, extending along the diagonal direction of the wall web, as shown in Fig. 8(a). Afterward, the horizontal shear reinforcement and boundary longitudinal reinforcement yielded at the same lateral drift, followed by crushing of boundary concrete, as shown in Fig. 8(d). Therefore, the failure mode of HPCW2 was defined as shear-compression failure. Although the yielding of boundary longitudinal reinforcement was observed for specimens HPCW0 and HPCW2, the yielding of boundary longitudinal reinforcement was in tension for HPCW0 caused by flexural mechanism while in compression for HPCW2 caused by shear-compression mechanism.

### *3.2. Lateral load-displacement responses*

Fig. 12 presents the lateral load-displacement hysteretic response for the three wall specimens. The points corresponding to the yielding of boundary longitudinal rebars, yielding of vertically and horizontally distributed rebars, and yielding of boundary transverse rebars can also be identified in Fig. 12. In addition, the flexural strength capacity $V_{\mathrm{fl}}@M_{\mathrm{n}}$, $V_{\mathrm{fl}}@M_{\mathrm{y}}$ and $V_{\mathrm{fl}}@M_{\mathrm{p}}$, and shear strength capacity $V_{\mathrm{s}}$ are also plotted in Fig. 12. The $V_{\mathrm{fl}}@M_{\mathrm{n}}$, $V_{\mathrm{fl}}@M_{\mathrm{y}}$ and

$V_{fl}$@$M_p$ corresponded to the cover concrete ultimate compressive strain of 0.003, first yielding of boundary longitudinal rebar, and peak flexural strength, respectively. The flexural strength capacity was calculated using the XTRACT program. The confined concrete model proposed by Saatcioglu and Razvi [25] was incorporated for boundary core concrete to reflect the confinement effect provided by transverse reinforcement. The Kent-Park model [26] was used for cover concrete and web wall concrete. The measured uniaxial stress-strain curves of rebars and strands were used for the XTRACT analysis. In addition, the tension-flexure peak strength of HPCW0 and HPCW1 was controlled by the fracture of strands due to their low uniform elongation, as listed in Table 1.

The shear strength capacity $V_n$ was calculated based on the design equations specified in ACI 318-19 (U.S. code) [22] and JGJ 3-2010 (China code) [17], as presented in Table. 3. In ACI 318-19 code formulae, the influence of axial compressive load on the shear strength of a PC wall is not considered directly, while a net axial tension is used in calculating the tension-shear strength of a PC wall subjected to axial tension. In JGJ 3-2010 code formulae, the net axial load is used in calculating the shear strength of a PC wall subjected not only to axial compression but also axial tension.

**Table 3.** Design formulae for shear strength of PC wall.

| Design code | Design formulae |
|---|---|
| ACI 318-19 (U.S.) [22] | $V_n = \left(\alpha\sqrt{f_c^{'}} + \rho_h f_{yh}\right) A_g$ <br> Where: $\alpha$=0.25 for $\lambda \leq 1.5$; $\alpha$ = 0.17 for $\lambda \geq 2.0$; $\alpha$=0.17(1+0.29$N/A_g$) for wall subjected to a net axial tension |
| JGJ 3-2010 | $V_n = \frac{1}{\lambda - 0.5}\left(0.4 f_t b_w h_{w0} + 0.1N\right) + 0.8 f_{yh} \frac{A_{sh}}{s} h_{w0}$ |

| |
|---|
| (China) [17] |

Where $V_n$ denotes the shear strength of the PC wall, $f_c$' denotes the compressive strength of concrete in MPa; $\rho_h$ denotes the ratio of horizontally distributed rebars; $f_{yh}$ denotes the yield strength of horizontally distributed rebars; $A_g$ denotes the gross area of wall section; $\lambda = Mh_{w0}/V$ denotes the shear-to-span ratio of the wall; $N$ is the total axial force of the wall concrete, including the prestressed force, which is positive for compression and negative for tension; $f_t$ denotes the axial tensile strength of concrete; $b_w$ denotes the wall thickness and $h_{w0}$ denotes the effective sectional depth of the wall; $s$ denotes the vertical spacing of horizontally distributed rebars; $A_{sh}$ denotes the area of horizontally distributed rebars within the spacing $s$.

The following observations can be made based on the results presented in Fig. 12: (1) For specimen HPCW0 which had a constant axial tensile force and exhibited flexure-shear failure, the hysteretic curves remained stable even under the large drift and the peak load was attained after yielding of boundary longitudinal rebars followed by horizontally and vertically distributed rebars. It is important to note the boundary longitudinal rebars yielded by tension for specimen HPCW0. Although specimen HPCW0 had a constant axial tension, its hysteretic curves in the positive and negative directions exhibited somewhat asymmetric. This is due to the cracks were asymmetrically distributed after applying the axial tension, as presented in Section 3.1. (2) For specimen HPCW1 which had a variable axial load, the hysteretic curves differed substantially in two loading directions due to the asymmetric loading pattern. The hysteretic curves displayed significant strength degradation in negative loading (coupled axial compression-shear loading direction) due to concrete crushing and longitudinal rebar buckling on the east wall boundary, and no obvious strength degradation in the positive direction (coupled axial tension-shear loading direction) until the cessation of testing. Furthermore, the yielding of reinforcement first occurred by tension in positive loading, and thereafter by compression in negative loading. (3) For specimen HPCW2 which had a constant axial compression force, the hysteretic curves were full and exhibited rapid post-peak strength degradation due to serious concrete crushing of both wall boundaries. The boundary longitudinal rebars and horizontally distributed rebars yielded at approximately the same lateral drift. Note that the boundary longitudinal rebars yielded by compression for specimen HPCW2 due to high axial compressive force ratio (the true axial compressive ratio was 0.45), as presented in Fig. 12(b). (4) A notable phenomenon was that lateral load increased along with a simultaneous decrease in axial tensile force and lateral drift was observed for specimen HPCW1 in the positive unloading stage, as shown in the *BC* phase in Fig. 12(b). This is because the increase in wall lateral capacity caused by a decrease in axial load exceeded the decrease in wall lateral capacity induced by the decrease in lateral drift. (5) Although flexural yielding strength $V_{\mathrm{fl}}$ @ $M_{\mathrm{y}}$ and flexural strength $V_{\mathrm{fl}}$ @ $M_{\mathrm{n}}$ ($\varepsilon_{\mathrm{c}}$=0.003) were attained for the three wall specimens, shear-controlled failure was observed for HPCW0 and HPCW2. This is because the strong boundary elements provided substantial flexural strength capacity, which is more prone to develop inclined shear cracks on the wall web and trigger shear-dominated failure, even after the yielding of boundary longitudinal reinforcement and cover concrete attained a compressive strain of 0.003. However, for HPCW1 which had a variable axial load, the buckled boundary reinforcement (as presented in Fig. 10(c)) in the coupled axial compression-shear loading direction was attributed to the fracture of boundary reinforcement in the coupled axial tension-shear loading direction, which led to a flexure-controlled failure. (6) The calculated tension-shear strength based on two design codes formulae were highly similar and significantly underestimated the tension-shear strength of PC walls with an experimental-calculated strength ratio of 2.46. The compression-shear strength calculated by ACI 318-19 (U.S. code) formulae was smaller than that of JGJ 3-2010 (China code) formulae because the influence of axial compression on the compression-shear strength of PC walls was not considered in ACI 318-19. The two design equations also significantly underestimated the compression-shear strength with experimental-to-calculated strength ratios of 1.58 and 2.06, respectively. This is because the strong boundary element and vertical strands also increase the shear strength capacity of PC walls, but were not considered in these equations. (7) XTRACT provided a reasonable estimation of the tension-flexure peak strength of PC walls subjected to coupled variable axial load and horizontal shear loading.

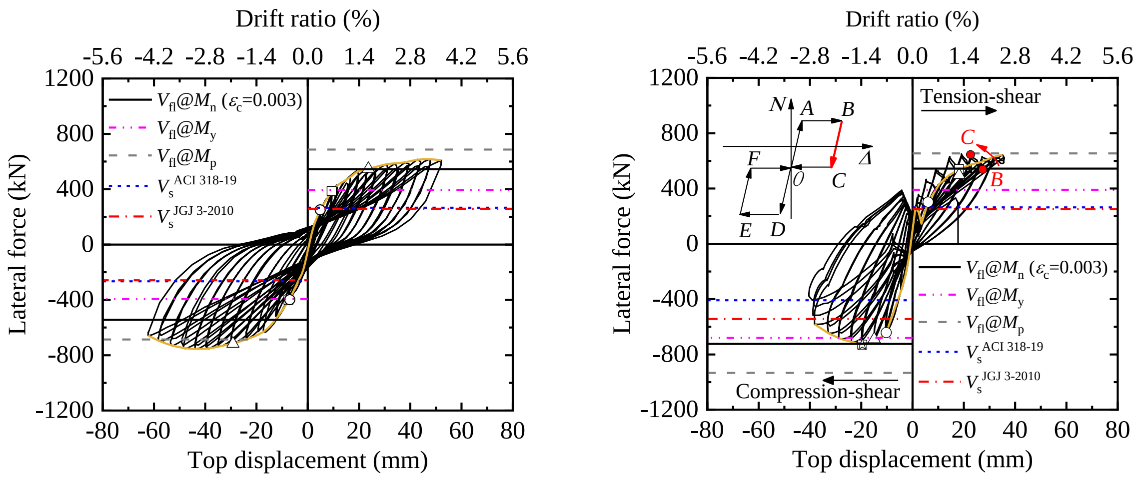


（a）HPCW0 （b）HPCW1

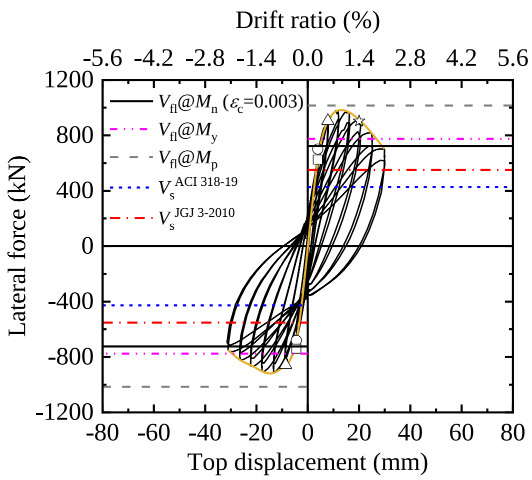


（c）HPCW2

| | | | |
|---|---|---|---|
| ☆ | Yielding of boundary transverse rebar | ○ | Yielding of boundary longidudinal rebar |
| □ | Yielding of horizontally dirtributed rebar | △ | Yielding of vertically dirtributed rebar |

**Fig. 12.** Lateral force versus top displacement response for all test walls.

*3.3. Lateral strength and deformation capacities*

Table 4 illustrates the measured yield load ($V_y$), corresponding to yield drift ($\Delta_y$) and yield drift ratio ($\theta_y$), the peak load ($V_p$), corresponding to peak drift ($\Delta_p$) and peak drift ratio ($\theta_p$), the normalized peak lateral load ($V_p/A_g\sqrt{f_c'}$), the ultimate drift ($\Delta_u$), and ultimate drift ratio ($\theta_u$). The measured yield point was determined using the idealized force-displacement curve method in accordance with ASCE/SEI 41-13[19]. Ultimate drift was defined as the post-peak drift at the instant when the lateral load decreases to 85% of the peak load. The values of $\theta_u$ of specimens HPCW0 and HPCW2 listed in Table 4 are the average values of ultimate drift ratio in positive and negative loading. For specimen HPCW1, where the lateral load increased during the unloading stage (*BC* phase in Fig. 12(b)), the peak load was defined as the maximum lateral load in the loading phase.

The following observations can be derived from Table 4. (1) Compared with specimen HPCW0 and HPCW2 which had a constant axial load, the normalized peak strength of HRCW1 with variable axial load decreased by 8.5 % and 9.1% in positive loading (coupled axial tension-shear loading) and negative loading (coupled axial compression-shear loading), respectively. (2) Compared with specimen HPCW0 which was subjected to constant tensile force, the ultimate drift ratio of specimen HPCW1 with variable axial forces decreased by 35% in tension-shear loading. This is likely to be attributable to the boundary longitudinal rebar that buckled in prior compression-shear loading and easily fractured in reversed tension-shear loading. The three wall specimens had ultimate drift ratios ranging from 1.8% to 3.7%, exceeding the elasto-plastic drift ratio limit of 1/100 specified in the Chinese design code (GB 50010-2010). (3) Although specimens HPCW1 and HPCW2 had compression-shear peak strengths of $0.70\sqrt{f_c^{'}}A_g$ and $0.77\sqrt{f_c^{'}}A_g$ which exceeded the limited value of $0.66\sqrt{f_c^{'}}A_g$ specified in ACI 318-19 [22] to guard against diagonal-compression failure, no diagonal-compression failure was observed in these tests, indicating that the limited value may be conservative for PC walls. A similar phenomenon was also observed for RC walls in prior studies in which the ratio of wall length to boundary element length was less than 6.0 (the ratio was equal to 3.0 for specimens HPCW1 and HPCW2 in this study) [27,23].

**Table 4.** Lateral strength and deformation capacities of test walls.

| Spec.no | Direction | $\Delta_y$ (mm) | $\theta_y$ (%) | $V_y$ (kN) | $\Delta_p$ (mm) | $\theta_p$ (%) | $V_p$ (kN) | $\frac{V_p}{A_g\sqrt{f_c^{'}}}$ | $\Delta_u$ (mm) | $\theta_u$ (%) |
|---|---|---|---|---|---|---|---|---|---|---|
| HPCW0 | W+ | 10.3 | 0.72 | 491.6 | 47.8 | 3.32 | 617.9 | 0.59 | 47.8 | 3.7% |
| | E- | -10.8 | -0.75 | -629.7 | -44.0 | -3.06 | -755.4 | | -58.3 | |
| HPCW1 | W+ | 10.1 | 0.70 | 448.4 | 35.1 | 2.44 | 594.2 | 0.54 | 35.1 | 2.4% |
| | E- | -8.8 | -0.61 | -696.9 | -19.6 | -1.36 | -779.1 | -0.70 | -33.6 | 2.3% |

| | | | | | | | | | | |
|---|---|---|---|---|---|---|---|---|---|---|
| HPCW2 | W+ | 4.6 | 0.32 | 819.2 | 11.9 | 0.83 | 979.9 | 0.77 | 25.5 | 1.8% |
| | E- | -5.2 | -0.36 | -791.3 | -13.3 | 0.92 | -915.4 | | -26.7 | |

# 4. Discussion of test results

## *4.1 Stiffness degradation and accumulated energy*

Fig. 13 presents the peak-to-peak lateral secant stiffness degradation and normalized lateral secant stiffness degradation (normalized by the calculated elastic lateral stiffness $K_0$) for the three wall specimens. (1) Before approximate yield drift ratio of 0.7%, specimen HPCW1 which had variable axial forces showed more pronounced stiffness degradation in tension-shear loading than that of specimen HPCW0 which had constant tensile force. Thereafter, the difference in stiffness degradation was less pronounced between specimens HPCW0 and HPCW1. It needs to note that compared with other specimens, specimen HPCW1 which had variable axial forces showed sharply lateral secant stiffness degradation in the first three loading levels. This is because in the first three loading levels, the target axial force corresponding to lateral drift levels changed from compression (first loading level) to tension (second and third loading levels), as shown in Fig. 5(b). (2) Specimen HPCW2, which had constant axial compressive force, exhibited more pronounced stiffness degradation than specimen HPCW1 in negative loading (coupled axial compression-shear loading). (3) The lateral secant stiffness at yield drift ($\Delta/\Delta_y$ = 1.0, $\Delta_y$ is the yield drift) was 0.18 and 0.67 of the calculated elastic lateral stiffness for specimens HPCW0 (coupled constant axial tension-shear loading) and HPCW2 (coupled constant axial compression-shear loading). The lateral secant stiffness values of the two specimens were the average values measured in positive and negative loading. For specimen HPCW1 that had a coupled variable axial loading and cyclic lateral loading, the lateral secant stiffness at yield drift was 0.12 and 0.28 of the calculated elastic lateral stiffness in tension-shear and compression-shear loading directions, respectively. Although the specimen HPCW1 in the compression-shear loading direction had an identical axial compressive force as specimen HPCW2, the former had an obvious lower lateral secant stiffness than that of specimen HPCW2. This is because each loading cycle of HSCW1 was comprised of the axial tension-shear loading followed by axial compression-shear loading, and the cracks developed in the preceding tension-shear loading resulted in a decrease of lateral secant stiffness in the followed compression-shear loading. (4) With the increasing lateral drift, the lateral secant stiffness of specimens HPCW0 and HPCW1 was approximately identical at two times yield drift ($\Delta/\Delta_y = 2.0$). The lateral secant stiffness was 0.08, 0.09, and 0.28 of the calculated elastic lateral stiffness for specimens HPCW0, HPCW1 and HPCW2, respectively at three times yield drift ($\Delta/\Delta_y = 3.0$).

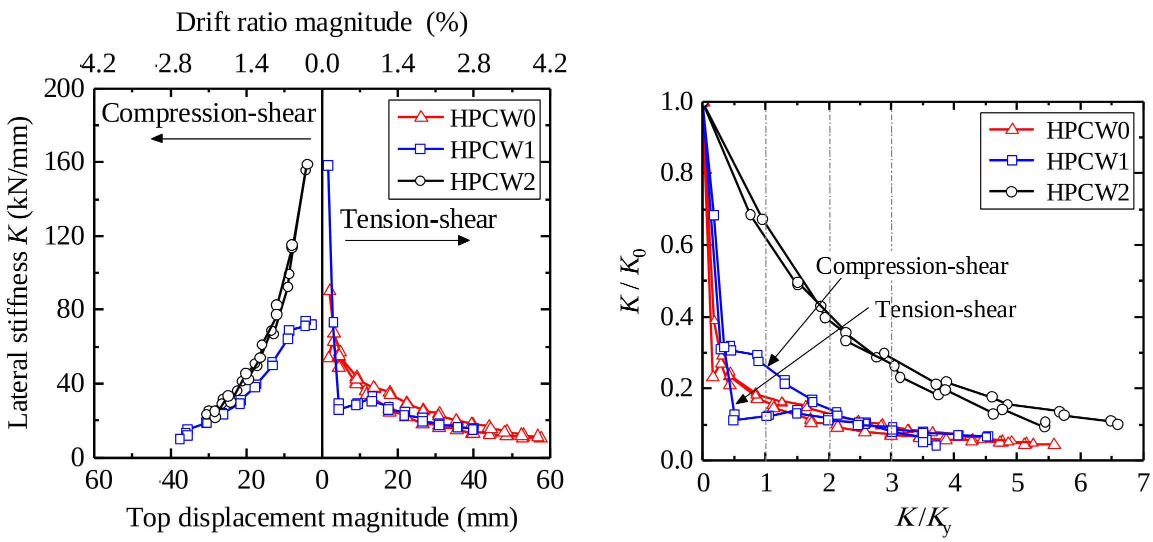


(a) Lateral scant stiffness

(b) Normalized lateral stiffness

**Fig. 13.** Lateral scant stiffness degradation for all test walls.

Fig. 14 presents a comparison of the accumulated energy dissipation for the three wall specimens, which were obtained by calculating the area enclosed in the hysteretic loops. As shown, although variable axial load had a limited influence on the lateral peak strength of the PC short-leg wall (as discussed in section 3.3), the accumulated energy dissipation of specimen HPCW1 with variable axial load was significantly smaller than that of specimens HPCW0 and HPCW2. This indicated that the variable axial load decreased the accumulated energy consumption dissipation of the PC short-leg wall. This is because the variable axial load changed the shape of the hysteretic loops of HPCW1 (as shown in Fig. 12(b)), resulting in a small area enclosed in these loops, especially in positive loading (coupled axial tension-shear loading).

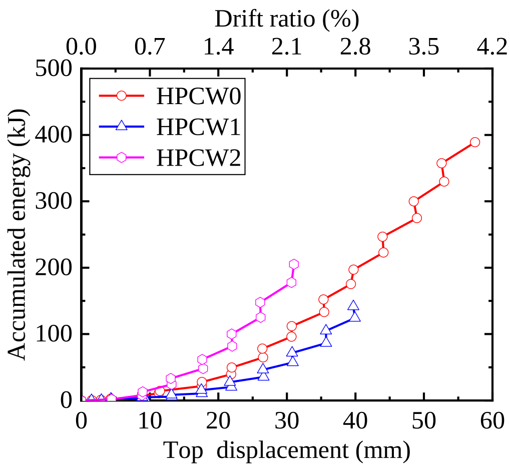


**Fig. 14.** Accumulated energy dissipation for wall specimens.

*4.2 Maximum crack width*

Fig. 15 presents the measured maximum crack width values at the peak load of the first cycle at each lateral drift level. The widest cracks in Fig. 15 are inclined cracks on the wall web mainly caused by coupled axial force and shear mechanism. The values for specimen HPCW0 and HPCW2 were the average values measured in positive and negative loading. As indicated in Fig. 15, the maximum crack width for each wall specimen increased approximately linearly as lateral drift increased, which is consistent with prior studies for RC members under the coupled axial compression-flexure-shear [28]. The maximum crack width of specimen HPCW1 in negative loading (couple axial compression-shear loading) was slightly smaller than that of specimen HPCW2, indicating that variable axial load had a limited influence on the maximum crack width of a PC wall subjected to axial compression and cyclic shear loading. In addition, the maximum crack width of specimen HPCW1 in positive loading (couple axial tension-shear loading) was significantly smaller than that of specimen HPCW0 which had constant axial tension. To summarize, the variable axial load did not increase the maximum crack width of PC walls. Except for specimen HPCW0 which had a constant axial tension, the maximum crack width of the other wall specimens was significantly less than 1.0 mm (which is the limiting value for considering repairability in AIJ code [29]) at the elasto-plastic drift ratio limit of 1.0% specified in the Chinese design code (GB 50010-2010) [18]. This indicates that the damage to the two other wall specimens after 1.0% drift loading was reparable.

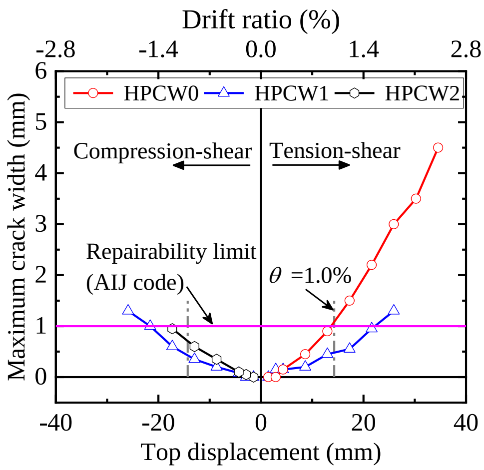


**Fig. 15.** Maximum crack width for all test walls.

*4.3 Deformation components*

Fig. 16 depicts the calculated methods of flexural and shear deformations. The flexural deformations were computed by integrating the rotations calculated from the LVDTs along both wall edges (D5 to D10 in Fig. 4) using the equation (1)-(2) proposed by Massone and Wallace [30]. The shear deformations were computed for each region by two pairs of inclined LVDTs (D11 to D14 in Fig. 4) using equation (1)-(2) also proposed by Massone and Wallace [30]. The wall lateral deformation resulting from reinforcement strain penetration at the wall-foundation interface was not calculated separately but was instead included in the flexural component because it was extremely difficult to quantify.

$$\mathit{\Delta} = \mathit{\Delta}_{\mathrm{f}} + \mathit{\Delta}_{\mathrm{s}} = \sum_{i=1}^{n} \mathit{\Delta}_{\mathrm{f},i} + \sum_{i=1}^{n} \mathit{\Delta}_{\mathrm{s},i} \tag{1}$$

$$\mathit{\Delta}_{\mathrm{f},i} = \xi \frac{\left(\delta_{\mathrm{R},i} - \delta_{\mathrm{L},i}\right)}{L} h_i + \sum_{j=1}^{i-1} \frac{\left(\delta_{\mathrm{R},j} - \delta_{\mathrm{L},j}\right)}{L} h_i \text{ ; } \quad \mathit{\Delta}_{\mathrm{s},i} = \frac{\sqrt{\left(\delta_{\mathrm{RS},i}\right)^2 - \left(d_{R,i}{}^2\right)} - \sqrt{\left(\delta_{\mathrm{LS},i}\right)^2 - \left(d_{L,i}{}^2\right)}}{2} - \mathit{\Delta}_{\mathrm{f},i} \tag{2}$$

Where, $\mathit{\Delta}$ denotes the total lateral displacement; $\mathit{\Delta}_{\mathrm{f}}$ denotes the total flexural displacement; $\mathit{\Delta}_{\mathrm{s}}$ denotes the total shear displacement; $\mathit{\Delta}_{\mathrm{f},i}$ and $\mathit{\Delta}_{\mathrm{s},i}$ denote the flexural and shear displacement at the $i_{\mathrm{th}}$ region, as shown in Fig. 16(a); $\delta_{\mathrm{R,i}}$ and $\delta_{\mathrm{L,i}}$ denote the vertical deformation of each wall side at the $i_{\mathrm{th}}$ reigion which can be measured by LVDTs (D5 to D10 in Fig. 4), as shown in Fig. 16(b); $\delta_{\mathrm{RS},i}$ and $\delta_{\mathrm{LS},i}$ denote the diagonal lengths for $X$ configuration at the $i_{\mathrm{th}}$ region which can be calculated using the test data of LVDTs (D11 to D14 in Fig. 4), as shown in Fig. 16(b); $d_{\mathrm{R,i}}$ and $d_{\mathrm{L,i}}$ denote the vertical lengths of each wall side at the $i_{\mathrm{th}}$ region which can be calculated using test data of LVDTs (D5 to D10 in Fig. 4), as shown in Fig. 16(b); $h_{\mathrm{i}}$ denotes the height of the $i_{\mathrm{th}}$ region; $L$ denotes the wall depth; $\xi$ is a factor and is taken as 0.67 [30].

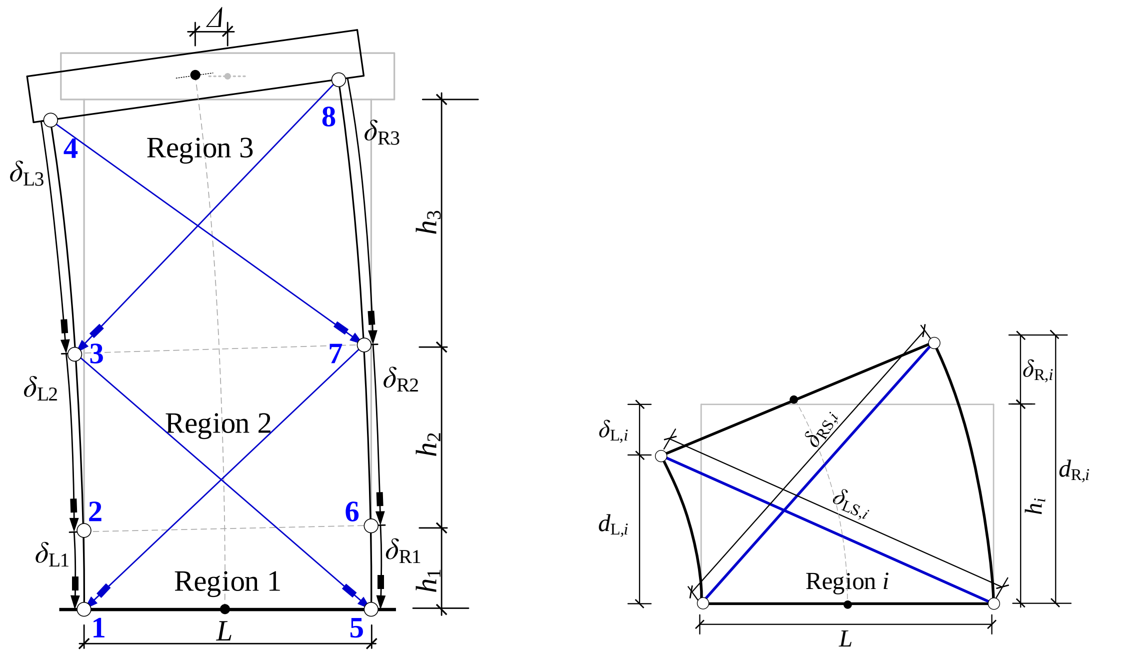


(a) Lateral deformation (b) Flexural and shear deformation at $i_{\mathrm{th}}$ region

Fig.16 Calculation of flexural and shear deformations

Fig. 17 depicts the contributions of flexural and shear deformations at the first cycle of each lateral drift level. The following observations can be made regarding the results presented in Fig. 17: (a) The contribution of shear deformations to top displacement tended towards continuous growth with the increasing lateral top displacement for all test walls, which was due to the development of inclined cracking and spalling of web concrete, and yielding of horizontally distributed rebars (as discussed in section 3). (b) For specimen HPCW0 which had a constant axial tension and exhibited flexure-shear failure, the shear deformation contribution increased as lateral displacement increased and exceeded 60% of lateral top displacement at the peak lateral load. (c) For specimen HPCW1 which was subjected to variable axial forces, the shear deformation contributed approximately 38% and 27% of lateral top displacement at the peak lateral load in the positive and negative loading directions, respectively. (d) For specimen HPCW2 that had a constant axial compression, the shear deformation contributed only 22% of lateral top displacement at the peak lateral load, significantly smaller than that of specimen HPCW0. This is because the axial tension led to more cracks and larger crack widths for specimen HPCW0 which decreased the shear stiffness and therefore resulted in larger shear deformation. This is consistent with the past finding by Beyer et al. [31, 32] that the axial tension increases the shear deformation contribution of RC walls.

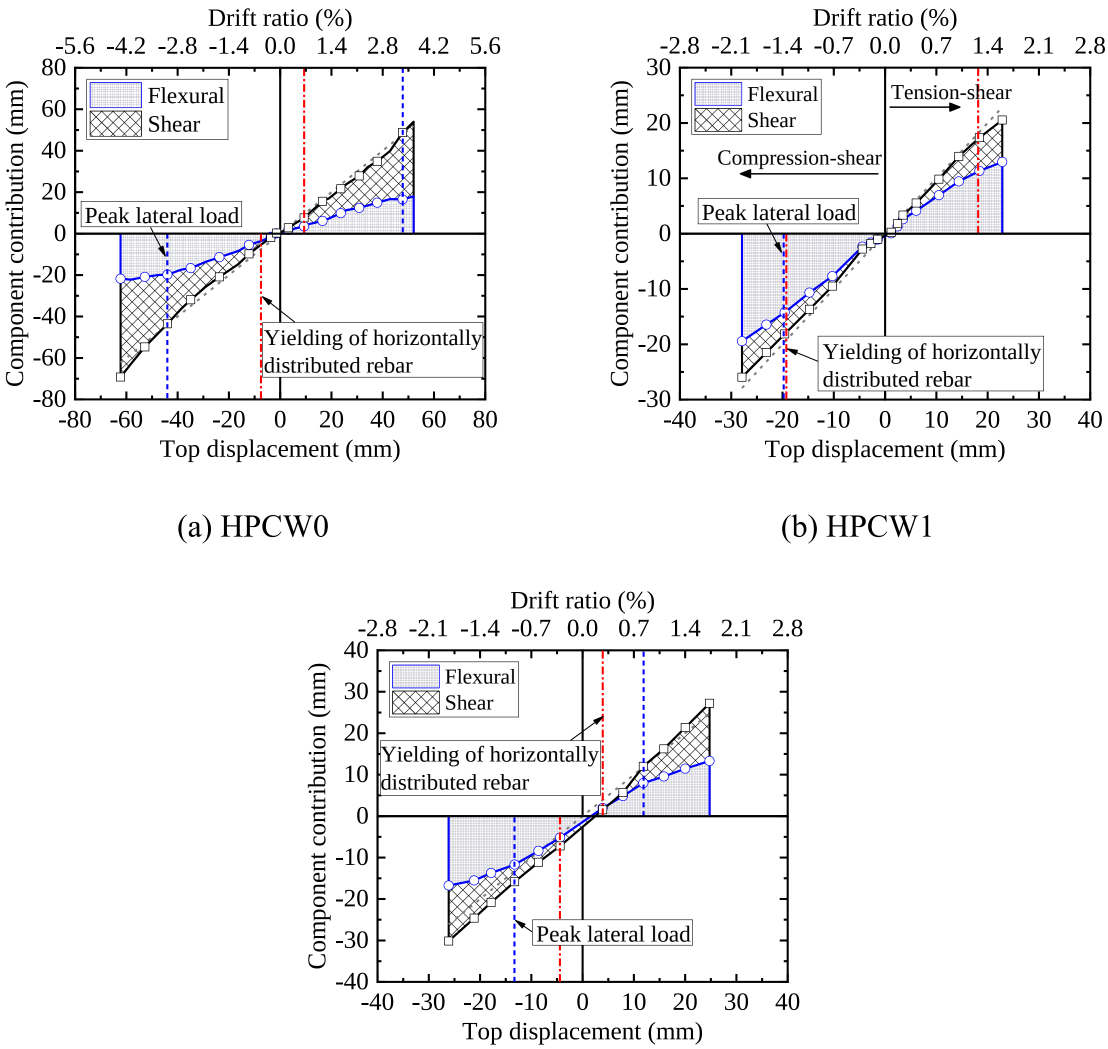


(a) HPCW0

(b) HPCW1

(c) HPCW2

**Fig. 17.** Deformation components for all test walls.

### *4.4. Axial deformation*

Fig. 18 presents the measured axial deformation versus top displacement relationship for the three wall specimens. The axial deformation responses of each wall specimen at 1.8% lateral drift are highlighted to illustrate the characteristics of axial deformation response of PC walls under different loading patterns. The positive axial deformation was axial elongation, while negative axial deformation was axial shortening. The following observations can be made regarding the results presented in Fig. 18: (a) For specimen HPCW0 which had a constant axial tension, the maximum axial deformation magnitude at each peak lateral displacement appeared to linearly increase as lateral displacement increased. This is consistent with previous test results of RC shear walls under constant axial tension [9, 33]. (b) For specimen HPCW1 which had a variable axial load, the axial deformation responses were markedly different in two loading directions due to the asymmetric loading pattern, as presented in Fig. 18(b). The increasing rate of axial elongation deformation in the *OA* and *BC* phase in which the axial load and lateral load changed simultaneously was larger than that in *AB* and *CO* phase which had a constant axial load. (c) For specimen HPCW2 which had a higher axial compressive force, the wall specimen gradually shortened as lateral displacement increased due to crushing and spalling of boundary concrete.

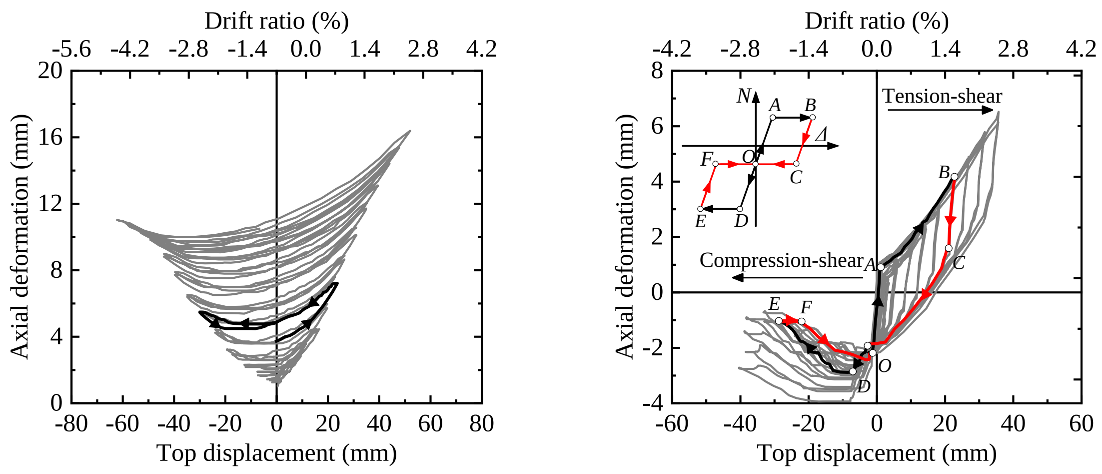


(a) HPCW0 (b) HPCW1

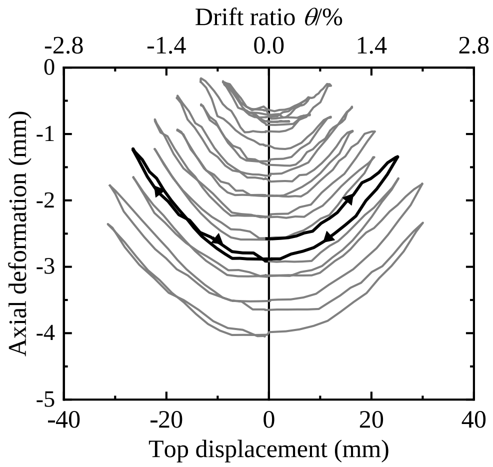


(c) HPCW2

**Fig. 18.** Axial deformation versus top displacement response for all test walls.

## 5. Comparison between PC wall and RC wall specimens

Cheng et al. [9] conducted a series tests for coupled axial tension-flexure behavior of RC walls (HSW1 through HSW4) that had an aspect-ratio of 2.0. Specimen HSW4 had an approximately identical shear-to-span ratio, reinforcement ratio, and normalized concrete tensile stress $n_t$ to specimen HPCW0 in this study, as presented in Table 4. After applying the axial tensile force, dense horizontal cracks were observed on the RC wall specimen HSW4, with a maximin crack width of 6.5 mm as shown in Fig. 19(a). However, the PC wall specimen HPCW0 had a maximum crack width of 0.1 mm, which was significantly smaller than that of HSW4 due to the existence of initial prestressed force. When subjected to cyclic shear loads, the RC wall specimen HSW4 failed by fracture of boundary longitudinal reinforcement due to a high axial tensile force, as presented in Fig. 19(b), whereas the PC wall specimen HPCW0 failed by flexure-shear failure due to crushing and spalling of web concrete, as presented in Fig. 19(b). The initial compressive force provided by strands prevented the extremely high tensile strain demand on boundary longitudinal reinforcement induced by large axial tensile force, and thus ensured full development of the concrete compression strength capacity. The ultimate drift of HPCW0 reached 3.7%, significantly larger than the HSW4's ultimate drift of 1.3%.

**Table 4.** Comparison between slender RC wall and PC wall

| Spec. no | $\lambda$ | $n_t$ | Reinforcement ratio | | Failure modes | Ultimate drift ratio |
|---|---|---|---|---|---|---|
| | | | $\rho_v/\rho_h$ | $\rho_b$ | | |
| HSW4 | 2.0 | 1.7 | 0.58% / 0.56% | 2.3% | Flexure failure | 1.3% |
| HPCW0 | 2.0 | 2.1 | 0.45% / 0.42% | 3.1% | Flexure-shear failure | 3.7% |

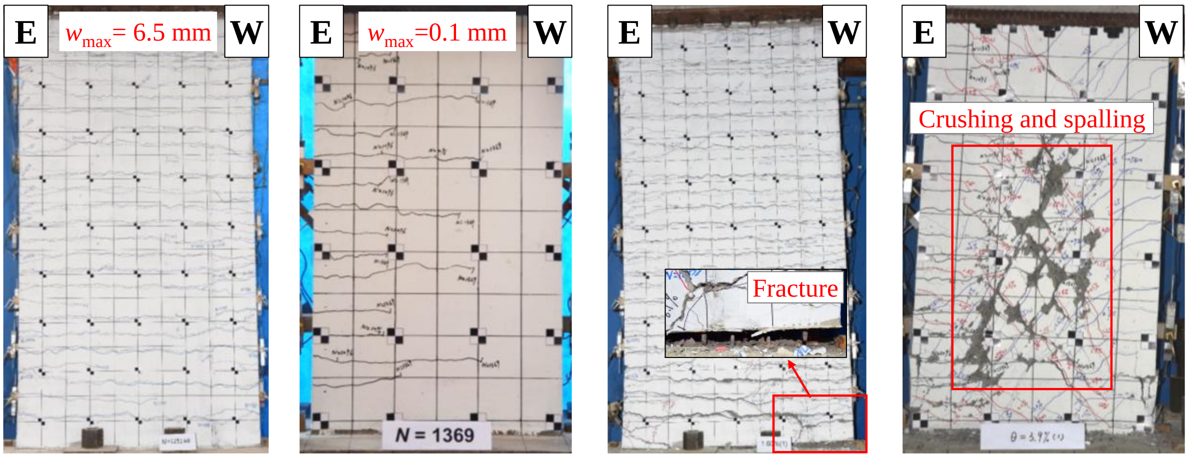


HSW4 HPCW0 HSW4 HPCW0

(a) After application of axial tensile force (b) After failure

**Fig. 19.** Photographs of RC wall and PC wall specimens

## 6. Numerical model for prestressed RC shear walls

### *6.1. Model description*

Unlike RC shear walls, numerical simulation of the seismic response of PC walls, especially for variable axial load, has seldom been reported in the literature. Therefore, in this study, a numerical model was developed to simulate the nonlinear cyclic response of PC walls subjected to various types of loading paths. The accuracy of the model in capturing the key response of PC walls was assessed by comparing it with the test results.

The numerical model was developed using the finite-element program OpenSees [34]. Fig. 20 presents a typical numerical model of PC walls. In this model, boundary elements were modeled using the displacement-based beam-column fiber element, which can ensure both reasonable levels of accuracy and convergence efficiency for shear walls with a high-aspect-ratio [35, 36]. The four-node plane-stress quad element with eight degrees of freedom (DOFs) was used to model the PC wall panel. The loading beam was simulated using elastic beam elements. The longitudinal reinforcement and strands embedded in boundary elements were represented by a number of discrete fibers of steel. The strands in the wall web were modeled using a two-node truss element. It is necessary to note that the high strength grouting material and corrugated pipes were not considered in this model for simplicity.

The unconfined concrete (concrete cover) and the confined concrete (confining effect induced by the stirrups) in boundary elements were simulated using a Concrete02 material model. The corresponding compressive stress and strain values at the peak and crushing point of unconfined concrete and confined concrete were calculated using the Scott-Kent-Park model [26] and Saatcioglu-Razvi model [25], respectively. The residual compressive strength was assumed to be 0.2 times the peak strength of the concrete. The longitudinal reinforcement and strands were simulated using the uniaxial Steel02 material model proposed by Menegotto and Pinto [37]. The values for yield strength $f_y$ and Young's modulus $E_0$ were determined from the rebar tensile tests, as presented in Table 2. The strain-hardening ratio $b$ equaled 1.0%. The parameters controlling the cyclic stiffness degradation characteristics of this model were calibrated as $R_0$ = 18.0, c$R_1$ = 0.925, and c$R_2$ = 0.15, as recommended in OpenSees. The PC panel of the wall specimen adopted the plane stress RC material model, named FAReinforcedConcretePlaneStress in OpenSees, which is based on the Cyclic Softened Membrane Model (CSMM) proposed by Mansour and Hsu [38]. The cracked reinforced concrete was assumed to be a continuum material in the smeared crack model. The material properties were characterized by a set of smeared stress-strain relationships for the concrete and the steel. Further detailed information on the CSMM can be found elsewhere [38]. The buckling and low-cycle fatigue of reinforcement and strands were not considered in this model.

The connecting behavior between the PC panel and strands in the wall web was simulated using the command “equalDOF”. This was also used to model the deformation compatibility between the boundary elements and the web elements. All nodes at the base of the model were entirely fixed. After trying various mesh sizes, the mesh size depicted in Fig. 20 was sufficient to obtain the required accuracy and improve the convergence efficiency. The axial load were applied to the nodes of the loading beam. In addition, the compressive force to wall induced by the pre-tension of strands were applied to the loading beam nodes, while the prestressed stress of strands was deducted from the yield strength of strands in the numerical model.

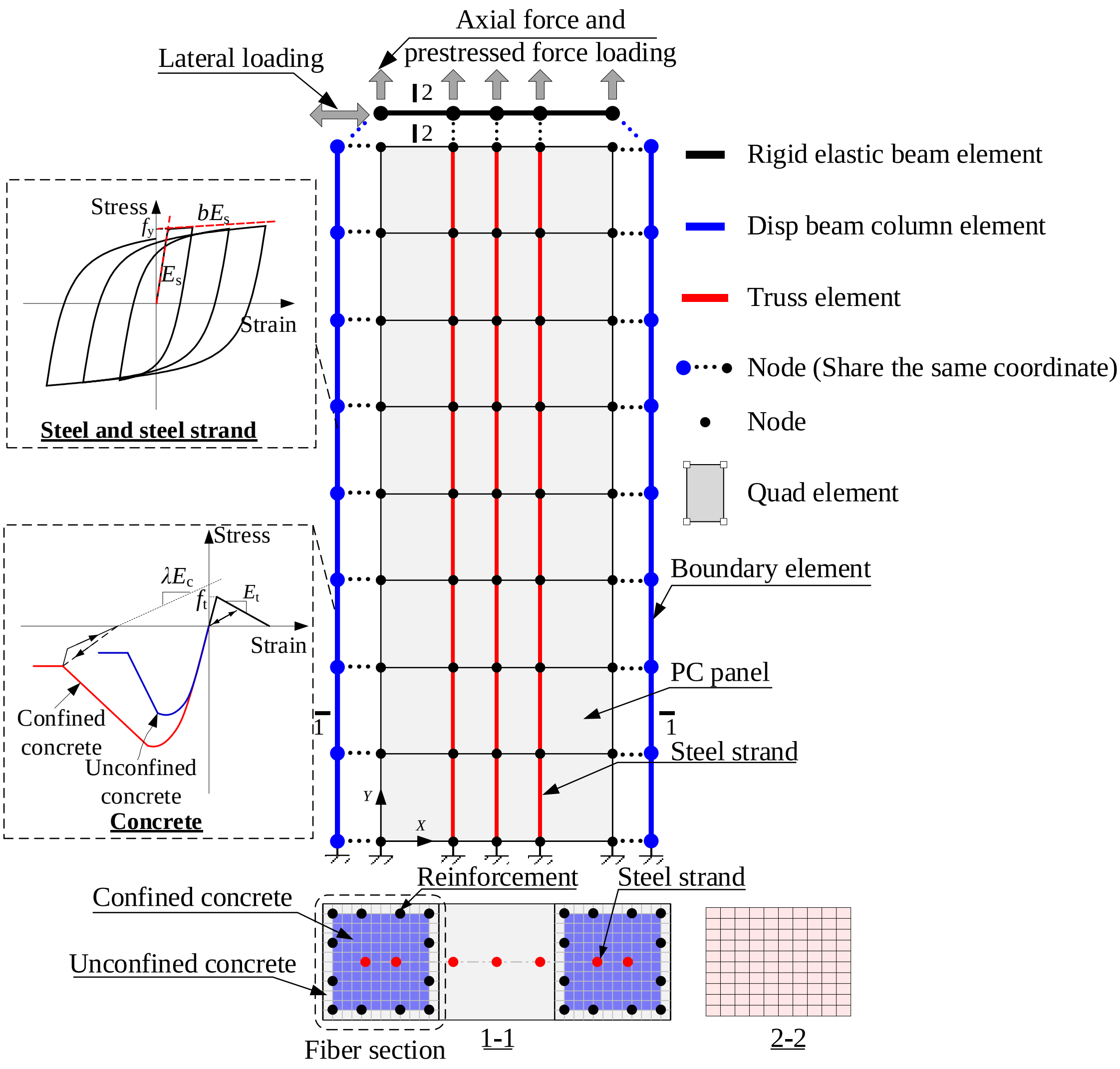


**Fig. 20.** Numerical model of PC wall.

*6.2. Verification of the numerical model*

*6.2.1 Lateral force-top displacement response*

Fig. 21 presents a comparison between the measured and predicted lateral force-top displacement hysteretic loops of all test wall specimens. In general, the numerical models were able to capture the general hysteretic responses of PC short-leg walls with reasonable accuracy, not only for wall specimens under a constant axial load but also under a variable axial load, including the peak lateral strength, initial stiffness, and cyclic pinching behavior for most of the applied lateral drift levels. The error of peak lateral strength between experimental and predicted results was typically less than 10% ( Note: the error values are the average values under positive and negative loading). Furthermore, the numerical model also predicted to a reasonable level the deformation capacity because it captured the cracking and crushing of concrete in the wall boundary regions and wall web, which was primarily responsible for initiating the experimentally-observed strength degradation. In particular, the numerical model captured the phenomenon of specimen HPCW1 whereby the lateral load increased when the axial tensile force and lateral drift decreased simultaneously, as depicted in the *BC* phase in Fig. 21(b).

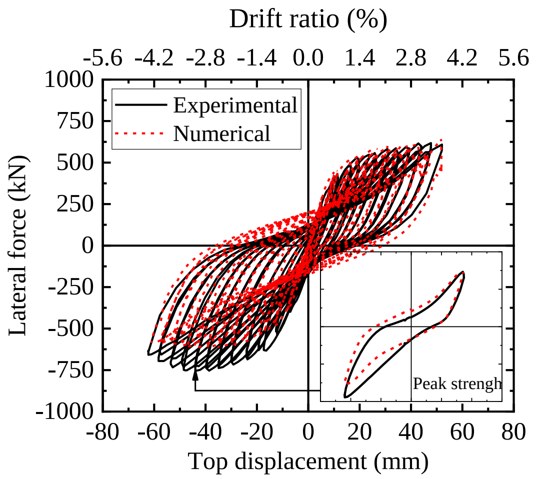


(a) HPCW0

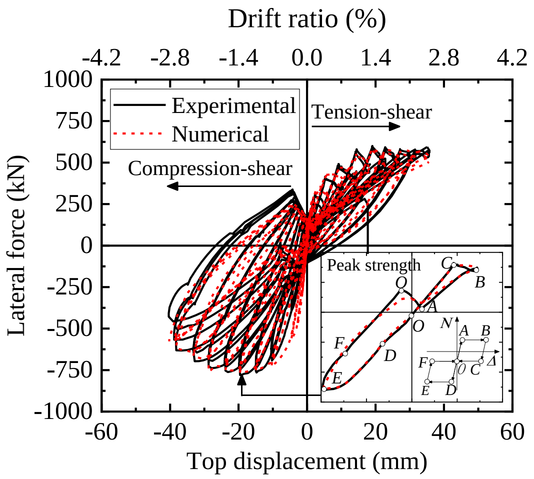


(b) HPCW1

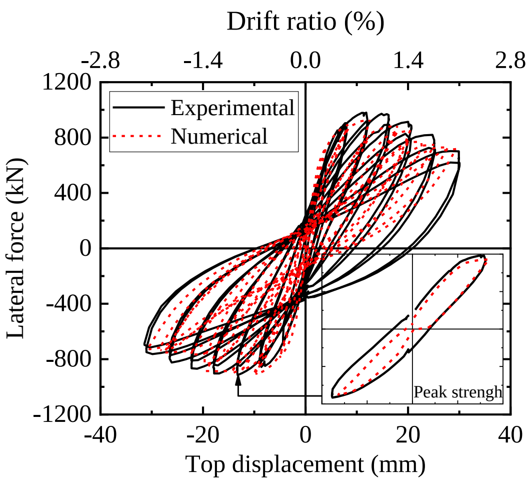

(b) HPCW2

**Fig. 21.** Comparison of the hysteretic response for all test walls.

*6.2.2 Lateral displacement distribution*

Comparisons of measured and predicated lateral displacement distribution profiles along the height of all wall specimens at 0.6% and 1.2% lateral drift are illustrated in Fig. 22. The displacement profiles were generated at peak top displacements during the first loading cycle for both measured and predicted results. The shape of the measured and predicted lateral displacement distribution profiles matched reasonably well, demonstrating that the numerical model captured the experimentally-observed lateral deformations along with the wall height. The lateral displacement deformation profiles were almost linear along with wall height for 0.6% and 1.2% lateral drift for specimen HPCW0 that was subjected to constant axial tension and failed due to crushing of web concrete, indicating that shear deformation was relatively larger for the wall specimen. This is consistent with the analytical results of deformation components presented in Fig. 17(a). For specimens HPCW1 and HPCW2 which exhibited flexure and shear compression failure, respectively, slightly nonlinear lateral deformations were observed within the bottom region of the wall because flexural deformation was relatively larger for the two specimens. This is also consistent with the analytical results of deformation components presented in Fig. 17(b)-(c).

Experimental, $\theta = 0.6\%$; Numerical, $\theta = 0.6\%$; Experimental, $\theta = 1.2\%$ Numerical, $\theta = 1.2\%$

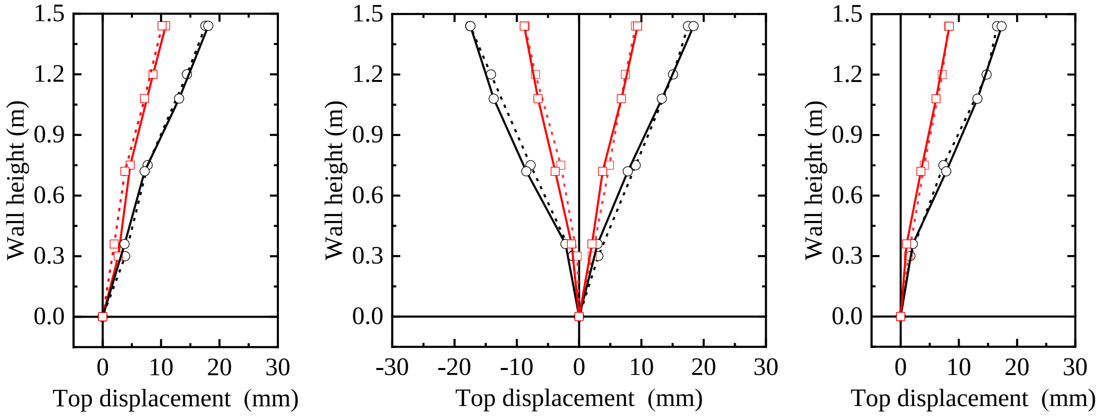


(a) HPCW0 (b) HPCW1 (c) HPCW2

**Fig. 22.** Comparison of the lateral displacement response for all test walls.

*6.2.3 Axial deformation responses*

Fig. 23 compares the measured and predicted axial deformation responses for all test wall specimens. The numerical model was capable of capturing the axial deformation response of specimens HPCW1 and HPCW2, including the maximum axial deformation magnitude at each peak lateral displacement and the residual axial deformation at zero lateral displacement. For specimens HPCW2 and HPCW1, the wall gradually shortened in coupled compression-shear loading due to the crushing of wall boundary concrete, which was also represented in this numerical result (as shown in Fig. 23(b)-(c)). Specimen HPCW0 shows different axial elongation in the positive and negative loading directions, while the numerical model only accurately predicts the axial elongation in the negative loading. The axial elongation of specimen HPCW0 in positive loading was larger than that in the negative loading, especially at large drifts. Such difference was related to unsymmetrically distributed horizontal cracks that were developed during the application of axial tensile force and caused by non-uniformly distributed restraint forces to foundation beams, as shown in Fig. 6(a) and discussed in

Subsection 3.1. The horizontal cracks concentrated at the east wall boundary significantly developed and widened when loading in the positive direction (loading to the west direction), which led to an increased axial elongation in positive loading. Because the numerical model assumed an ideal boundary condition that did not consider the non-uniformly distributed restraint forces to foundation beams, it produced nearly identical axial elongation in both loading directions.

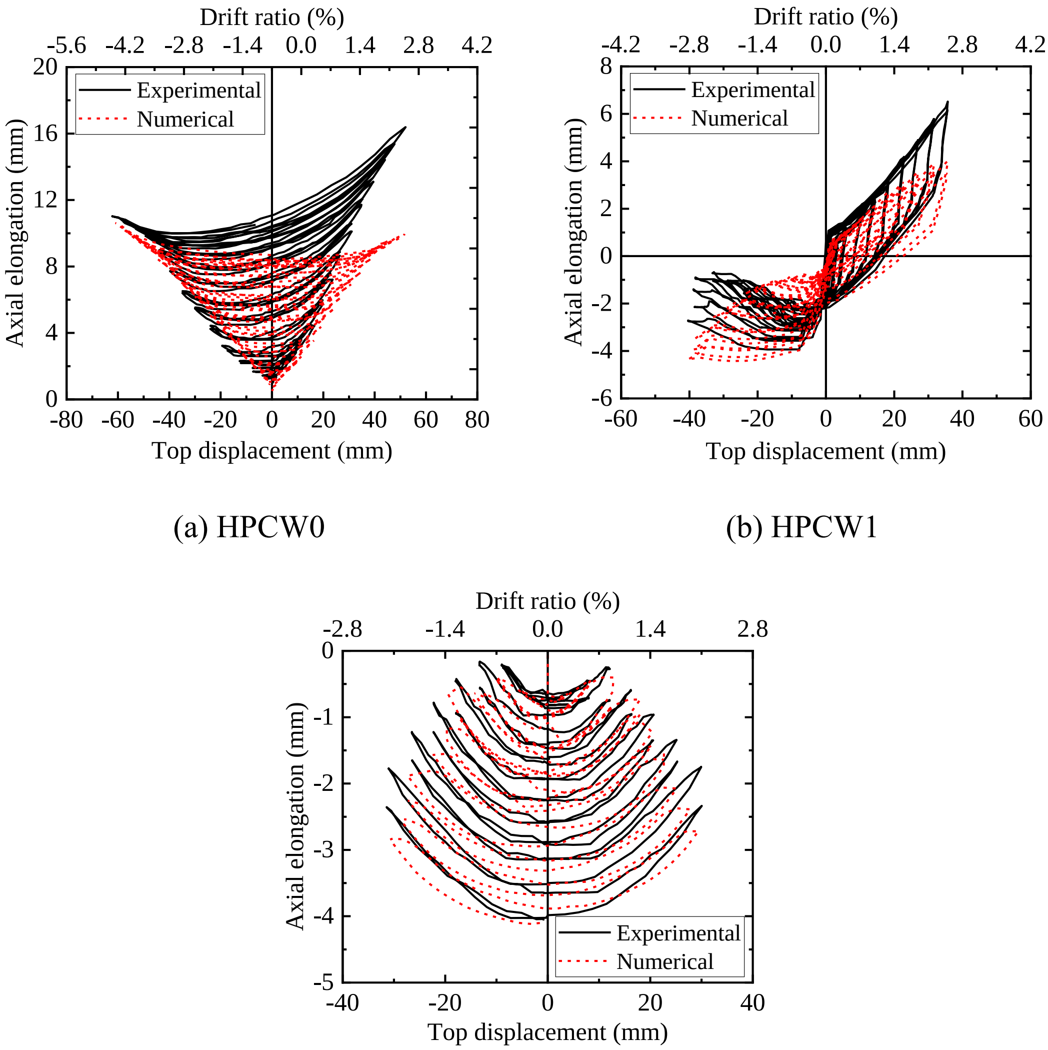


(a) HPCW0 (b) HPCW1

(c) HPCW2

**Fig. 23.** Comparison of the axial deformation for all test walls.

In addition, the calculated strains from the numerical model were also compared with the measured strain data (e.g., the strains of boundary longitudinal reinforcement). It indicates that while the model can reasonably track the measured strains for the specimens at low drifts, it cannot accurately predict the strains at large drifts, because it cannot simulate the buckling of reinforcement. Because the test specimens are limited, the numerical model will be further validated and developed using more test data in the future.

## 7. Conclusions

An experimental study was conducted to investigate the seismic behavior of high-aspect-ratio bonded prestressed concrete (PC) short-leg walls under various loading patterns. The major findings are summarized as follows:

(1) Loading patterns have significant effects on the failure patterns of PC short-leg walls. For a wall specimen subjected to constant axial tensile force (net normalized concrete tensile stress level $n_{t,tot} = 0.67$), a flexure-shear failure was observed due to web concrete crushing. For a wall specimen with constant axial compression (total axial compressive force ratio $n_{c,tot} = 0.45$), shear compression failure was observed due to boundary concrete crushing. For a wall specimen with variable axial load, flexure failure occurred due to boundary concrete crushing in the compression-shear loading direction, followed by fracture of boundary longitudinal rebars in the tension-shear loading direction.

(2) Loading patterns had significant effects on the hysteretic response of PC short-leg walls. Especially for wall specimen subjected to variable axial load, an interesting phenomenon that lateral load increased with a simultaneous decreasing of axial load and lateral drift was observed in the tension-shear unloading stage.

(3) Variable axial load decreased the normalized tension-shear and compression-shear strength

by 8.5% and 9.1%, respectively. In addition, the limited value specified in ACI 318-19 to guard against diagonal compression failure appeared to be conservative for PC short-leg walls.

(4) Variable axial load decreased the pre-yield secant stiffness in tension-shear and compression-shear loading, while the influence on post-yield secant stiffness was less pronounced. Variable axial load did not increase the maximum crack width of PC short-leg walls, but clearly decreased the accumulated energy dissipated by PC short-leg walls.

(5) Shear deformation contributed to more than 60% of lateral top displacement at the peak lateral load for a wall specimen exhibiting flexure-shear failure, but contributed to only 22% for wall specimens exhibiting shear compression failure. The shear deformation contributed approximately 38% and 27% of lateral top displacement at the peak lateral load in tension-shear and compression-shear loading, respectively, for wall specimens subjected to variable axial force.

(6) A numerical model was developed based on the cyclic softened membrane model to simulate the cyclic lateral response of PC short-leg walls, which can well simulate the global response PC short-leg walls with different loading patterns, including hysteretic response and lateral displacement profile.

**Acknowledgements**

The authors gratefully acknowledge sponsorship by the National Natural Science Foundation of China (Grant No. 52108429 and 52078277) and Beijing Nova Program (Grant No. Z211100002121097). The writers wish to express their sincere gratitude to the sponsors.

**References**

[1] A.S. Elnashai, B. Gencturk, O.S. Kwon, I.L. Al-Qadi, Y. Hashash, J. R. Roesler, S.J. Kim,

S.H. Jeong, J. Dukes, A. Valdivia, The Maule (Chile) earthquake of February 27, 2010: consequence assessment and case studies. Mid-America Earthquake Center. Report No: 10-04. University of Illinois at Urbana-Champaign, 2010.

[2] P. Xu, Y. Xue, C. Xiao, C. Wang, H. Sun, Z. Xu, R. Gu, Experimental study on seismic performance of high-rise SRC hybrid structures, Build. Struct. 35(5) (2005) 3–8. (in Chinese).

[3] Z. Yao, X. Fang, H. Wei, Experimental study on shear behavior of reinforced concrete shear walls under eccentric tension, J. Build. Struct. 41(4) (2020) 71–81. (in Chinese).

[4] T. Wang, T. Lai, H. Zhao, H. Lin, Y. Wang, Tensile-shear mechanical performance test of reinforced concrete shear wall, J. Build. Struct. 47(2) (2017) 64–69. (in Chinese).

[5] C. Ren, C. Xiao, P. Xu, Experimental study on tension-shear performance of reinforced concrete shear wall, Chin. Civi. Eng. J. 51(4) (2018) 20–33. (in Chinese).

[6] X. Ji, X. Cheng, M. Xu, Coupled axial tension-shear behavior of reinforced concrete walls, Eng. Struct. 167 (2008) 132–142.

[7] X. Nie, J. Wang, M. Tao, J. Fan, Experimental study of shear-critical reinforced-concrete shear walls under tension-bending shear-combined cyclic load, J. Struct. Eng. 146(5) (2020) 04020047.

[8] F. Wei, H. Chen, Y. Xie. Experimental study on seismic behavior of reinforced concrete shear walls with low shear span ratio. J. Build. Eng. 45 (2022) 103602.

[9] X. Cheng, X. Ji, R.S. Henry. Coupled axial tension-flexure behavior of slender reinforced concrete walls. Eng. Struct. 188 (2019) 261–276.

[10] CMC. Chinese Technical Guideline of Peer Review for Seismic Design of Super-Tall Buildings. Beijing: China Ministry of Construction, 2003. (in Chinese).

[11] X. Ji, Y. Sun, J. Qian, X. Lu, Seismic behavior and modeling of steel reinforced concrete (SRC) walls, Earthq. Eng. Struct. D. 44(6) (2015) 955–972.

[12] X. Ji, X. Cheng, X. Jia, A.H. Varma, Cyclic in-plane shear behavior of double-skin composite walls in high-rise buildings, J. Struct. Eng. 143(6) (2017) 04017025.

[13] X. Ji, T. Leong, J. Qian, W. Qi, W. Yang, Cyclic shear behavior of composite walls with encased steel braces, Eng. Struct. 127 (2016) 117–128.

[14] Y. Kurama, R. Sause, S. Pessiki, L.W. Lu, Lateral load behavior and seismic design of unbonded post-tensioned precast concrete walls, ACI Struct. J. 96(4) (1999) 622–632.

[15] T. Holden, J. Restrepo, J. Mander, Seismic performance of precast reinforced and prestressed concrete walls, J. Struct. Eng. 129(3) (2003) 286–296.

[16] R.S. Henry, Self-centering precast concrete walls for buildings in regions with low to high

seismicity. Ph.D. Dissertation. Univ. of Auckland, Auckland, New Zealand, 2011.
[17] CMC. Technical specification for concrete structures of tall building (JGJ 3-2010). Beijing: China Ministry of Construction; 2010 [in Chinese].
[18] CMC. Code for design of concrete structures (GB50010-2010). Beijing: China Ministry of Construction, 2010. (in Chinese).
[19] ASCE. Seismic rehabilitation of existing buildings. ASCE/SEI 41-13. Reston, VA: American Society of Civil Engineers; 2014.
[20] Y. Wan, Z. Xu, X. Ji, X. Cheng, T. Wang, Y. Zhao. Experimental study on cyclic shear behavior of low-aspect-ratio prestressed concrete walls under variable axial tension-compression forces. J Build Struc. (in Press)
[21] Imbsen and Associates Inc. XTRACT-Cross Section Analysis Program for Structural Engineers-Step by Step Examples, IMBSEN Software Systems v. 3.0.8, California, 2007.
[22] ACI 318-19. Building code requirements for structural concrete (ACI 318-19) and commentary. Farmington Hills (MI): American Concrete Institute, 2019.
[23] J. Moehle, Seismic design of reinforced concrete buildings. New York: McGraw-Hill Education, 2014.
[24] Paulay, T. and M. Priestley, Seismic design of reinforced concrete and masonry buildings. 1992. 1992: John Wiley and Sons, New York. 744.
[25] M. Saatcioglu, Razvi SR. Strength and ductility of confined concrete. J Struct Eng 1992; 118(6):1590–07.
[26] B. Scott, R. Park, M. Priestley. Stress-strain behavior of concrete confined by overlapping hoops at low and high strain rates. ACI Struct J 1982; 79(2): 13-27.
[27] E. Hines, F. Seible, Web crushing capacity of hollow rectangular bridge piers, ACI Struct. J. 101(4) (2004) 569–579.
[28] A. Borosnyói, G. Balázs, Models for flexural cracking in concrete: State-of-art, Struct. Concr. 6 (2005) 53–62.
[29] AIJ. Guidelines for Performance Evaluation of Earthquake-Resistant Reinforced Concrete Buildings (Draft). Architecture Institute of Japan, 2004.
[30] L. Massone, B. Sayre, J. Wallace, Load-deformation responses of slender structural steel reinforced concrete walls, Eng. Struct. 140 (2017) 77–88.
[31] K. Beyer, A. Dazio, M. Priestley. Quasi-static cyclic tests of two U-shaped reinforced concrete walls. J. Earthq. Eng. 12(7) (2008) 1023-1053.
[32] K. Beyer, A. Dazio, M. Priestley. Shear deformations of slender reinforced concrete walls under seismic loading. ACI Struct. J. 108(2) (2011) 167-177.

[33] X. Ji, Z. Miao, R. Kromanis. Vision-based measurements of deformations and cracks for RC structure tests. Eng. Struct. 212 (2020) 110508.

[34] F. McKenna, G. Fenves, M. Scott, Open system for earthquake engineering simulation. California: University of California Berkeley, 2000. http://opensees.berkeley.edu.

[35] Y. Mo, J. Zhong, T. Hsu, Seismic simulation of RC wall-type structures, Eng. Struct. 30 (2008) 3167–3175.

[36] B. Wang, H. Jiang, X. Lu, Seismic performance of steel plate reinforced concrete shear wall and its application in China Mainland, J. Constr. Steel Res. 131 (2017) 132–143.

[37] M. Menegotto, P.E. Pinto, Method of analysis for cyclically loaded reinforced concrete plane frames including changes in geometry and non-elastic behavior of elements under combined normal force and bending, In: Proceedings of the IABSE symposium on resistance and ultimate deformability of structures acted on by well defined repeated loads. Lisbon, (1973) 15–22.

[38] M. Mansour, T.T.C. Hsu, Behavior of reinforced concrete elements under cyclic shear: Part 2: theoretical model, J. Struct. Eng. 131(1) (2005) 54–65.